Supplementary Information

Enhancing Neutral Hydrogen Production by Disrupting the Rigid Hydrogen Bond Network on Ru Nanoclusters through Nb_2O_5-Mediated Water Reorientation

Xiao Hui Chen[a], Xiao Lin Li[a], Ting Li[a], Jia Huan Jia[a], Jing Lei Lei[b], Nian Bing Li[a,*], and Hong Qun Luo[a,*]

[a] *School of Chemistry and Chemical Engineering, Southwest University, Chongqing 400715, People's Republic of China*

[b] *School of Chemistry and Chemical Engineering, Chongqing University, Chongqing 400044, People's Republic of China*

[*]Corresponding author.

Nian Bing Li and Hong Qun Luo

E-mail address: linb@swu.edu.cn; luohq@swu.edu.cn

1. Experimental Section

1.1 Chemicals and reagents

Sodium dihydrogen phosphate dihydrate ($NaH_2PO_4 \cdot 2H_2O$), disodium hydrogen phosphate dodecahydrate ($Na_2HPO_4 \cdot 12H_2O$), potassium hydroxide (KOH), anhydrous oxalic acid ($H_2C_2O_4$), and methenamine ($C_6H_{12}N_4$) were purchased from Aladdin Co., Ltd. (Shanghai, China). Niobium pentachloride ($NbCl_5$) and ruthenium chloride hydrate ($RuCl_3 \cdot xH_2O$) were provided by Macklin Chemical Reagent Co., Ltd. (Shanghai, China). Pt/C (20 wt % Pt on Vulcan XC-72R) and Nafion (5 wt %) were purchased from Sigma-Aldrich Chemical Reagent Co., Ltd. (USA). Ethanol (C_2H_5OH) was produced from Chuandong Chemical Co., Ltd. (Chengdu, China). All chemicals were used as received without further purification. Deionized water (18.2 MΩ cm) was used throughout the experiments.

1.2 Preparation of pre Nb_2O_5

Specifically, 0.0818 g of $NbCl_5$ and 0.375 g of $H_2C_2O_4$ were added to 30 mL of deionized water and sonicated until the chemicals were completely dissolved. Next, 0.21 g of $C_6H_{12}N_4$ was then added to the above solution. Then the solution containing 3 cm × 3 cm of carbon cloth (CC) was transferred to a 50 mL Teflon-lined stainless steel autoclave and reacted at 180 °C for 12 h. After the reaction, the autoclave was naturally cooled to room temperature, and the Nb_2O_5 precursor grown on CC (Nb_2O_5-pre) was washed several times with ethanol and water, and then dried in vacuum. To prepare Nb_2O_5-2-pre, the amounts of $NbCl_5$, $H_2C_2O_4$, and $C_6H_{12}N_4$ need to be doubled, while keeping the rest of the conditions unchanged.

1.3 Preparation of Ru/Nb_2O_5

The Nb_2O_5-pre and Nb_2O_5-2-pre with dimensions of 1.0 cm × 3.0 cm were immersed in 4.0 mL of 0.5 mg mL^{-1} $RuCl_3•xH_2O$ solution for 12 hours to obtain Ru/Nb_2O_5-pre and Ru/Nb_2O_5-2-pre, respectively. Finally, the obtained precursor was calcined in an ammonia atmosphere by ramping up the temperature to 500 °C over 60 minutes and holding it at that temperature for 90 minutes to synthesize Ru/Nb_2O_5 and Ru/Nb_2O_5-2. The prepared Nb_2O_5-pre undergoes the same nitridation treatment to obtain Nb_2O_5.

1.4 Preparation of Ru

The CC with the dimensions of 1.0 cm × 3.0 cm was immersed in 4.0 mL of $RuCl_3•xH_2O$ solution with a concentration of 0.5 mg mL^{-1} and reacted at 60 °C for 12 hours to obtain Ru-pre. Subsequently, the Ru-pre undergoes the same nitridation treatment as the samples mentioned above to obtain Ru.

1.5 Preparation of H-Ru

The hydrothermal method for depositing Ru on CC (H-Ru) substrate was modified from the reported work.[1] 0.0295g of $CH_3COONa·3H_2O$ was added to 30.0 mL of 0.5 mg mL^{-1} $RuCl_3•xH_2O$ solution. After stirring evenly for 30 min, the homogeneous black solution was transferred to a 30 mL Teflon-lined stainless steel autoclave. The hydrothermal reaction was carried out for 8 h at the temperature of 180 °C. After the reaction was completed, anhydrous ethanol and ultra-pure water were used for washing 3 times respectively. Subsequently, the H-Ru precursor undergoes the same nitridation treatment as the samples mentioned above to obtain H-Ru.

1.6 Preparation of Pt/C electrode

The Pt/C control electrode was prepared by a drop-cast method. Specifically, 2.0 mg of the 20 wt.% Pt/C powder was added to 190 μL of H_2O and 50 μL of anhydrous ethanol, and then

ultrasonically dispersed for 20 minutes. After 10 μL of the Nafion solution (5 wt.%) was added to the suspension, ultrasonic agitation was continued for another 20 minutes. Subsequently, 50 μL of ink was dropped onto a 1 cm × 1 cm CC, which was then dried at 60°C. The same process was repeated for four times. The mass loading of Pt/C on CC is 1.6 mg cm^{-2}. The Pt mass loading of the electrode was 320 μg_{Pt} cm^{-2}. The benchmark Pt/C is stored in separate dry dishes, and clean spatulas are used for sampling when preparing Pt/C electrodes. Fresh electrolyte is used during electrochemical performance testing to ensure it is not contaminated.

2. Characterizations

The morphology of the obtained materials was observed by scanning electron microscopy (SEM, ZEISS Gemini 300, ZEISS, Germany) and transmission electron microscopy (TEM, Talos F200X, Thermo Fisher Scientific, USA). The crystalline structures of samples were identified by powder X-ray diffraction (XRD, X' Pert PRO, PANalytical B.V., Holland) using Cu-Kα radiation. The X-ray photoelectron spectroscopy (XPS) analysis was measured on Thermo Scientific K-Alpha using Mg-Kα radiation (Thermoelectricity Instruments, USA). Electron paramagnetic resonance spectra were collected on a Bruker A300-10/12 spectrometer (EPR, Bruker A300-10/12, Bruker, Germany) at room temperature. Atomic force microscopy was used to analyze the thickness of catalyst layers (AFM, Bruker Dimension ICON, Germany). The material from an area of 1.5 cm × 0.5 cm was ultrasounded in 4 mL of ethanol for 5 minutes, and the supernatant was dropped onto a silicon wafer. After drying at 60 °C, AFM measurement was conducted. The Raman spectra were measured on a Horiba Scientific LabRAM HR Evolution (HORIBA Jobin Yvon, France). The *in-situ* electrolytic cell used was provided by Beijing Scistar Technology Co. Ltd. (China). Inductively coupled plasma mass spectrometry (ICP-MS) characterization was performed on an Agilent Varian

720ES equipment (Agilent, USA). Ultrasound was used to detach Ru/Nb_2O_5 from the CC substrate, with a power of 100 W for 1 h. After drying the centrifuged powder, a certain amount of Ru/Nb_2O_5 was weighed and dissolved in aqua regia (V_{HNO3} : V_{HCl} = 1 :3) for ICP-MS analysis.

3. Electrochemical Measurements

Without specific instructions, all electrochemical measurements were performed using a CHI Electrochemical Workstation (Model 660E, Shanghai Chenhua Instrument Co., Ltd., China) in Ar-saturated 1.0 M PBS or 1.0 M KOH. A three-electrode system at room temperature was used, where the prepared catalysts on carbon cloth were used directly as the working electrode (0.5 cm^2 electrode area), and Ag/AgCl and graphite rod were used as reference electrode and counter electrode, respectively. The electrochemical impedance spectroscopy (EIS) measurements were performed at the perturbation of 5 mV amplitude in the range from 0.01 Hz to 100 kHz. The polarization curves with 80% *iR*-correction were recorded by linear sweep voltammetry (LSV) at a scan rate of 5 mV s^{-1}. The Tafel slopes were derived from a linear fit utilizing the Tafel equation ($\eta = b \log j + a$, where η is the overpotential, b is the Tafel slope, and j is the current density).

All the potentials were calibrated to the reversible hydrogen electrode (RHE) based on the equation (1).

$$E(RHE) = E(Ag/AgCl) + 0.0591 \bullet pH + 0.197 \quad \text{Eq. (1)}$$

The amount of generated H_2 was collected in the H-type of the electrolytic cell using the drainage method. The Faraday efficiency (FE) was acquired according to the following formula：

$$\mathrm{FE} = z \times n \times \frac{F}{I \times t} \times 100\% \quad \text{Eq. (2)}$$

where z is the electron transfer number (2), n is the amount (moles) of the generated gas in the experiment, F is the Faraday constant (96485.3 C mol^{-1}), I is the applied constant current (A), and t is the electrolysis time (s).

The H_2 amount was calculated from the volume of evolved H_2 based on the following equation:

$$n = \frac{V}{V_m} \qquad \text{Eq. (3)}$$

where V represents the collected volume of H_2; V_m represents the molar volume of the gas.

4. Surface-enhanced Raman spectroscopy (SERS)

We used electrochemically roughened gold (Au) as a substrate to achieve surface enhancement effect. Firstly, the Au was mechanically polished using alumina powder (1 μm), followed by multiple sonication steps in a 1:1 mixture of ethanol and acetone, and then in ultrapure water. The clean gold (Au) was subjected to 20 cycles of oxidation-reduction at a scan rate of 50 mV s^{-1} between -0.28 and 1.22 V *vs.* Ag/AgCl in a 0.1 M KCl solution. After the potential cycling, the Au surface was reduced for 5 min at a constant potential of -0.3 V *vs.* Ag/AgCl. Finally, the resulting brownish Au surface was thoroughly rinsed with ultrapure water.[2] We detached Nb_2O_5 and Ru/Nb_2O_5 from the CC substrate through ultrasonic treatment and then dropped them onto an Au electrode for *in situ* SERS measurements. The specific process is as follows：2.0 mg of the catalysts was added to 230 μL of anhydrous ethanol and 20 μL of Nafion solution (5 wt.%), and then ultrasonically dispersed for 20 minutes to obtain the catalyst ink. Dropping ink onto the pre-treated gold electrode, we controlled the catalyst mass loading to 1.6 mg cm^{-2}. Due to the low mass loading of Ru on CC (3.32 μg cm^{-2}) and its small particle size, it is not possible to obtain powder. Therefore, when testing in situ SERS of Ru, Au is sprayed onto the surface of Ru/CC.[3]

5. Ab initio molecular dynamics (AIMD) theoretical simulation

The first-principles-based molecular dynamics (MD) simulations were performed using CP2K code.[4] Firstly, the Ru_{13}, Nb_2O_5, and Ru_{13}/Nb_2O_5 models were constructed and optimized. Subsequently, a slab surface containing 60 water molecules was constructed. Before performing the molecular dynamics calculations, the system was equilibrated under the NPT ensemble (T=298 K, P=101 KPa) for 10 ps to reach an appropriate state. Then, a 5 ps simulation was conducted using the NVT ensemble. The force and velocity are calculated using density functional theory (DFT) for Perdew–Burke–Ernzerhof (PBE) functional, Gaussian-type basis set6 and Goedecker-Teter-Hutter (GTH) pseudopotentials combined with Gamma k-point and 400 Ry plane wave cutoff.[5] The temperature is controlled with a Nose−Hoover thermostat attached to every degree of freedom to ensure equilibration. The DFT-D3 dispersion correction method was used to describe the weak interaction between ions. The atomic models were described using VMD software. In the AIMD simulation, we imported the obtained structural files into VMD software and utilized the H-bond analysis tool to quantify the number of hydrogen bonds. In these three different AIMD scenarios, the Ru system uses the bottom Ru atom as the 'zero' point, while both bare Nb_2O_5 and Ru/Nb_2O_5 take the position of the top-layer atom on the Nb_2O_5 substrate surface as the 'zero' point.

6. Density functional theory (DFT) calculations

The Vienna Ab Initio Package (VASP) was employed to perform all the density functional theory (DFT) calculations within the generalized gradient approximation (GGA) using the Perdew, Burke, and Enzerhof (PBE) formulation.[6-8] The projected augmented wave (PAW) potentials were applied to describe the ionic cores and take valence electrons into account using a plane wave basis set with a kinetic energy cutoff of 450 eV.[9, 10] Partial occupancies of the Kohn–Sham orbitals were

allowed using the Gaussian smearing method and a width of 0.05 eV. The electronic energy was considered self-consistent when the energy change was smaller than 10^{-5} eV. A geometry optimization was considered convergent when the force change was smaller than 0.01 eV/Å. The vacuum spacing perpendicular to the plane of the structure is 15 Å. Brillouin-zone sampling was sampled with 2×2×1 Monkhorst-Pack grids. Two atomic layers contained the 3×1 Nb_2O_5 (001) slab. Thirteen Ru atoms are used to construct the Ru cluster model (Ru_{13}). A Ru_{13} cluster was placed on 3×1 Nb_2O_5 (001) slab to build the Ru/Nb_2O_5 heterojunction. The climbing image nudged elastic band (CI-NEB) and Dimer methods had been adopted to calculate dissociation barriers of H_2O in Ru_{13} cluster, Nb_2O_5 slab, and Ru_{13}/Nb_2O_5 heterojunction.

The Gibbs free-energy (ΔG) is calculated as follows:

$$\Delta G = \Delta E_{ads} + \Delta E_{ZPE} + T\Delta S \quad (4)$$

where ΔE_{ZPE} is the difference corresponding to the zero point energy between the adsorbed molecule and molecule in the gas phase, and ΔS is one molecule entropy between adsorbed state and gas phase.

The adsorption energy (ΔE_{ads}) is calculated using the expression:

$$\Delta E_{ads} = E_{molecule+surface} - E_{surface} - E_{molecule} \quad (5)$$

where $E_{surface}$ is the energy of Ru_{13} cluster, Nb_2O_5 slab, and Ru_{13}/Nb_2O_5 composite, $E_{molecule}$ represents the energy of the H* or H_2O, and $E_{molecule+surface}$ represents the total energy of the adsorbed system.

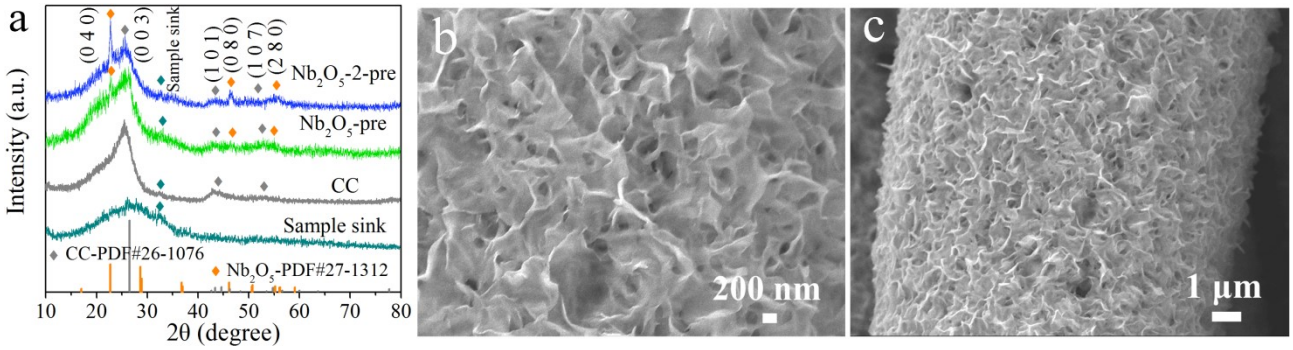

Fig. S1. (a) XRD patterns and (b, c) SEM images of Nb_2O_5-pre.

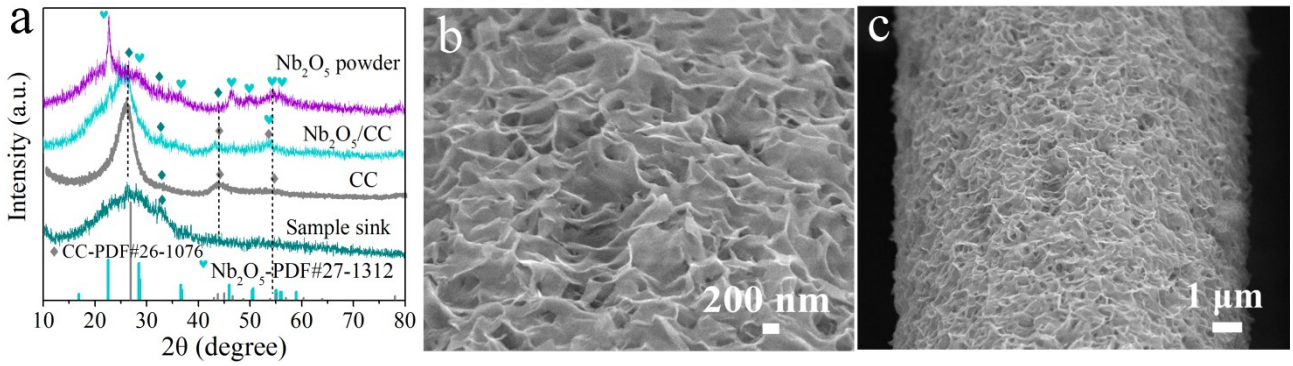

Fig. S2. (a) XRD patterns and (b, c) SEM images of Nb_2O_5 (obtained by high-temperature calcination of Nb_2O_5-pre in NH_3). Nb_2O_5 powder used in XRD was obtained from nitridating the residue remaining in the Teflon-lined stainless steel autoclave during the preparation of Nb_2O_5-pre/CC. The peaks of Nb_2O_5 powder at ~26° and ~44° are closer to the background interference caused by the sample holder. The peak at 54.5° can be attributed to the (2 8 0) crystal plane of Nb_2O_5.

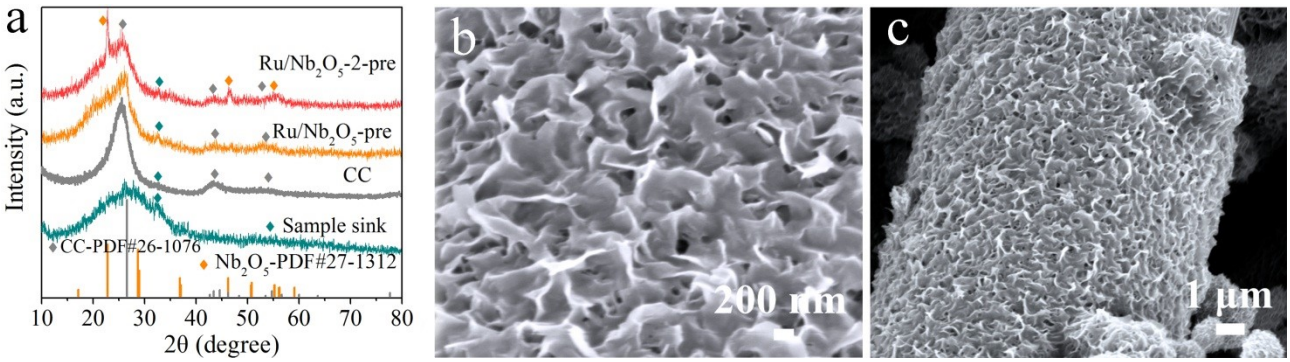

Fig. S3. (a) XRD patterns and (b, c) SEM images of Ru/Nb_2O_5-pre.

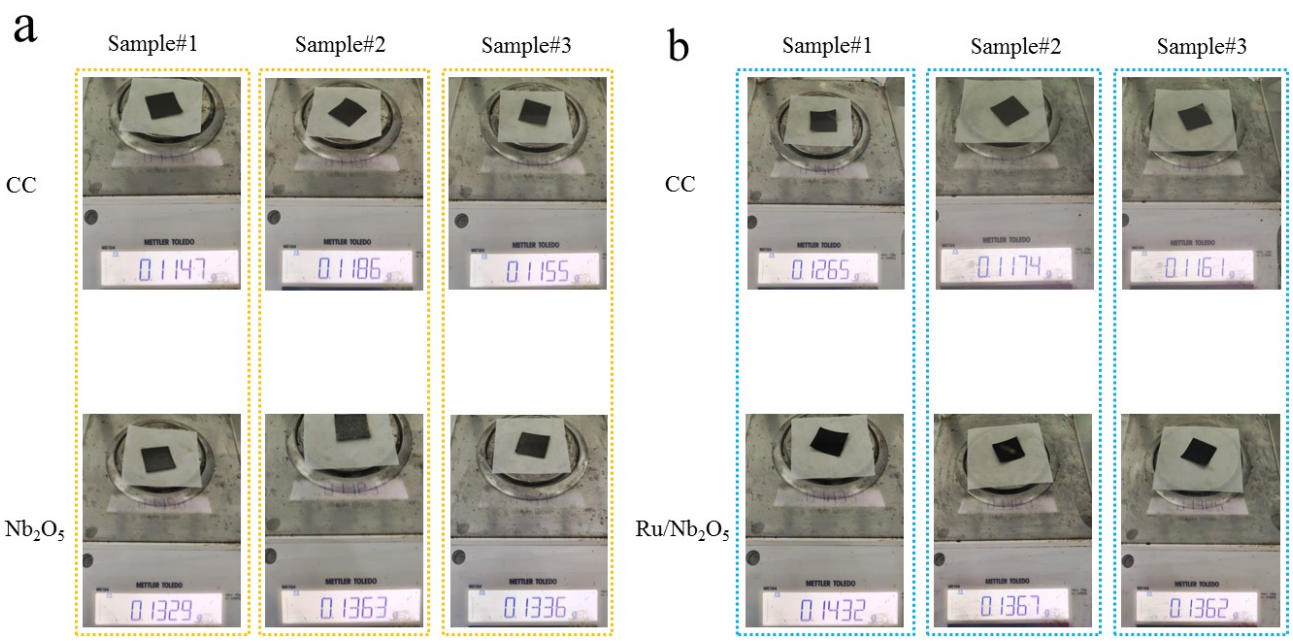

Fig. S4. The mass loading of (a) Nb_2O_5 and (b) Ru/Nb_2O_5. The average mass loading of Nb_2O_5 and Ru/Nb_2O_5 on CC (3 cm × 3 cm) is 0.0180 and 0.0187 g, respectively.

As shown in Fig. S4, the average mass loading of Nb_2O_5 and Ru/Nb_2O_5 on CC (3 cm × 3 cm) is 0.0180 and 0.0187 g, respectively. Therefore, the loadings normalized by the geometric surface area of the electrode for Nb_2O_5 and Ru/Nb_2O_5 are 2.00 and 2.08 $mg_{cat.}$ cm^{-2}, respectively.

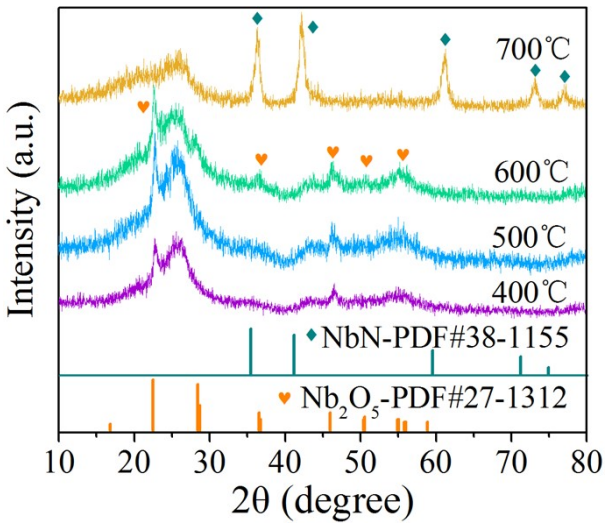

Fig. S5. XRD patterns of Ru/Nb_2O_5 prepared at different nitridation temperatures.

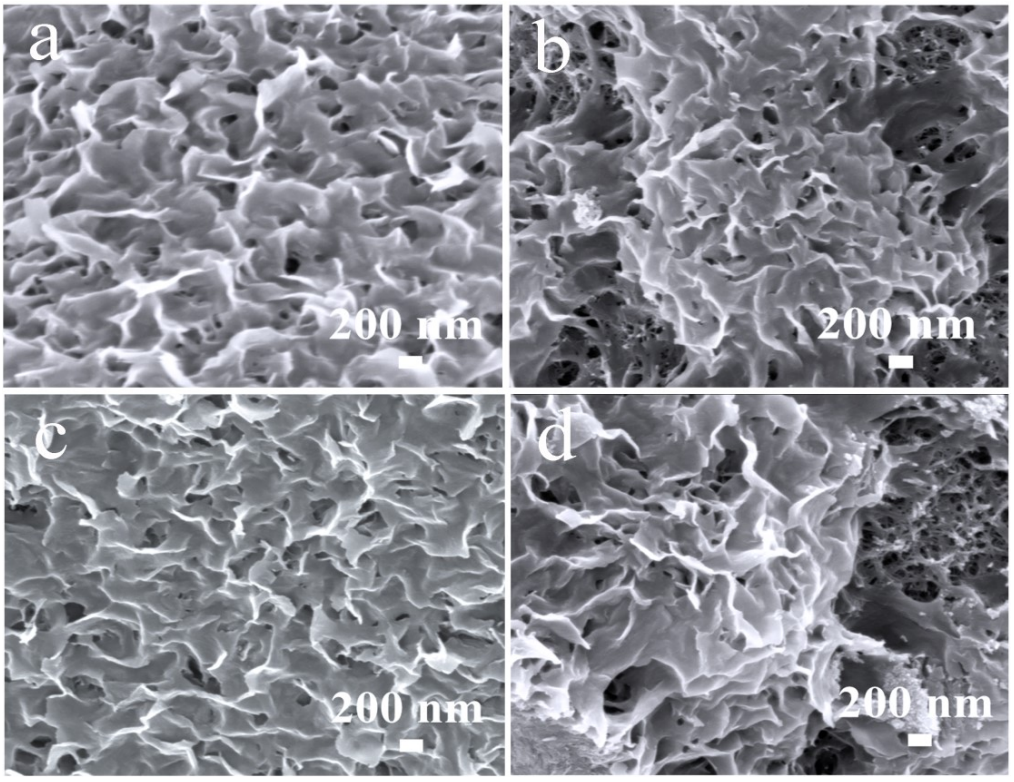

Fig. S6. SEM images of (a) Ru/Nb_2O_5-pre and Ru/Nb_2O_5 prepared at (b) 400 °C, (c) 500 °C, and (d) 600 °C.

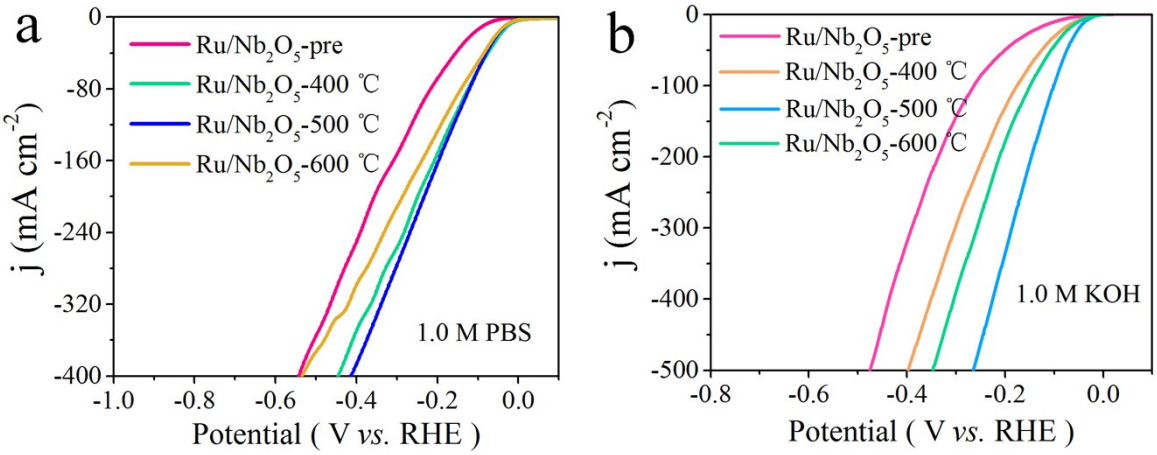

Fig. S7. LSV curves of Ru/Nb_2O_5 prepared at different temperatures in (a) 1.0 M PBS and (b) 1.0 M KOH.

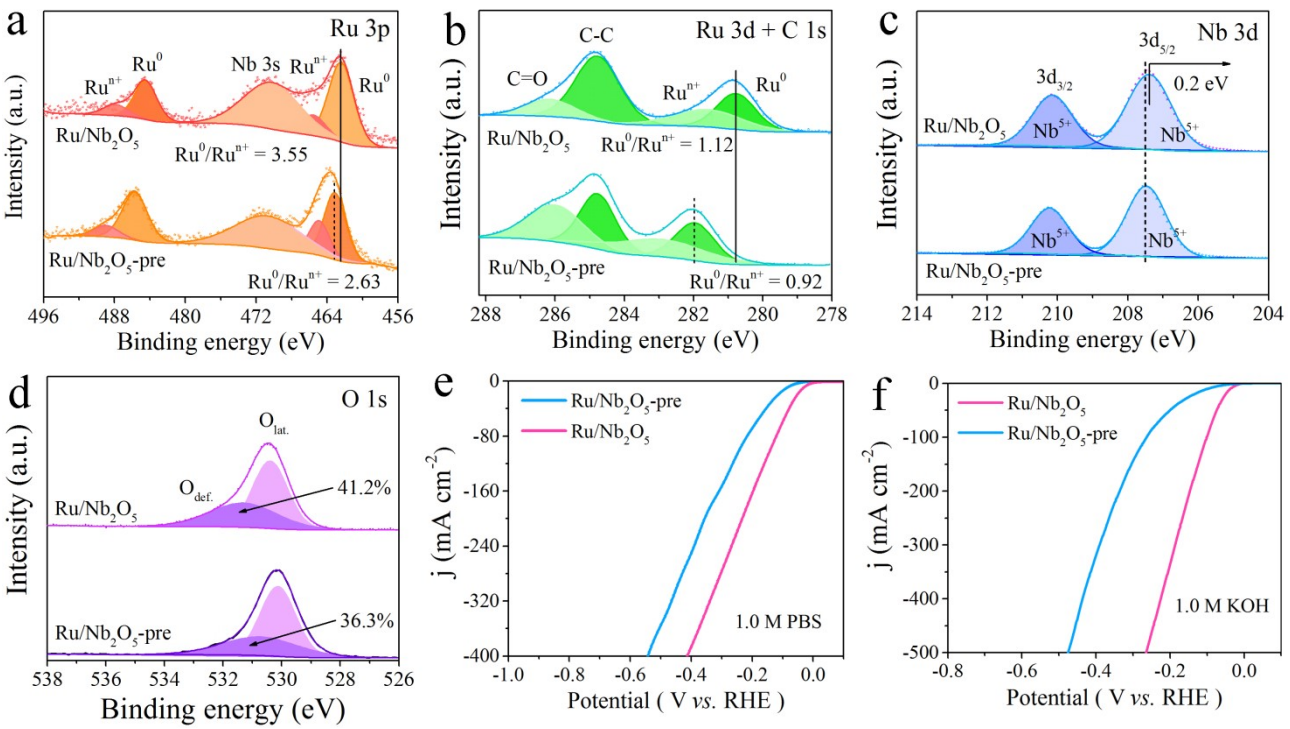

Fig. S8. High resolution XPS spectrum of (a) Ru 3p, (b) Ru 3d + C 1s, (c) Nb 3d, and (d) O 1s for Ru/Nb_2O_5 and Ru/Nb_2O_5-pre. LSV curves of Ru/Nb_2O_5 and its precursor in (e) 1.0 M PBS and (f) 1.0 M KOH.

After high-temperature treatment in NH_3, the binding energy of Ru^0 and Nb $3d_{5/2}$ decreases, while the ratio of Ru^0/Ru^{n+} increases. This indicates that the Ru/Nb_2O_5-pre has been reduced, and more oxygen defects (O_v) are generated simultaneously. Meanwhile, the catalytic performance of Ru/Nb_2O_5 has been enhanced in both neutral and alkaline solutions. The oxidation state of Nb in Ru/Nb_2O_5-pre and Ru/Nb_2O_5 is +5.[11, 12] The reason for the generation of O_v is that the H and N atoms in NH_3 were able to extract O atoms in Nb_2O_5 to form H_2O, N_2O, and NO. Therefore, Nb_2O_5 is converted to O_v-enriched Nb_2O_5 and metal nitrides sequentially with the increase in calcination temperature.[13, 14]

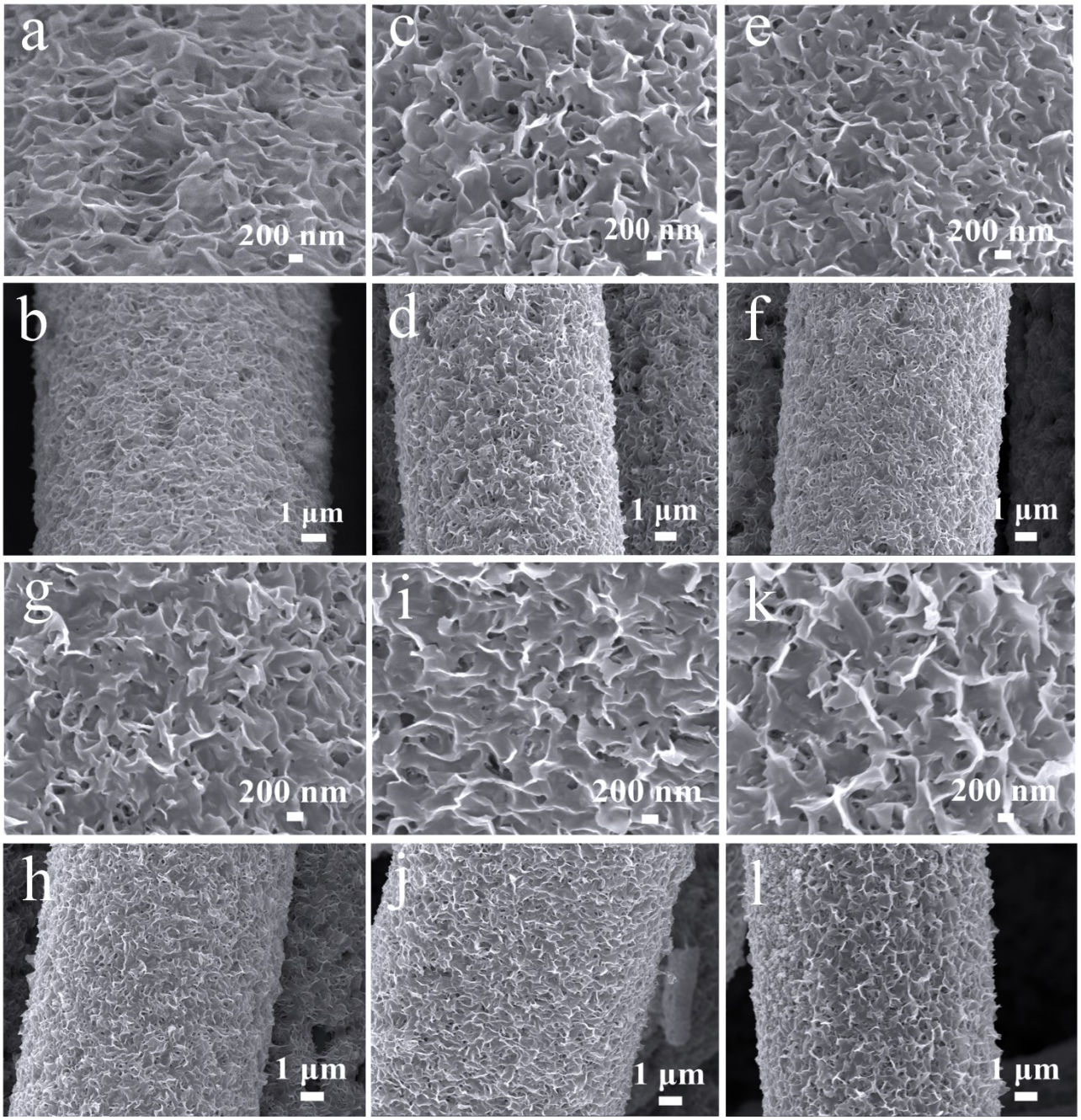

Fig. S9. SEM images of Ru/Nb_2O_5 with different soaking times: (a, b) 0 h, (c, d) 2 h, (e, f) 4 h, (g, h) 8 h, (i, j) 12 h, (k, l) 20 h.

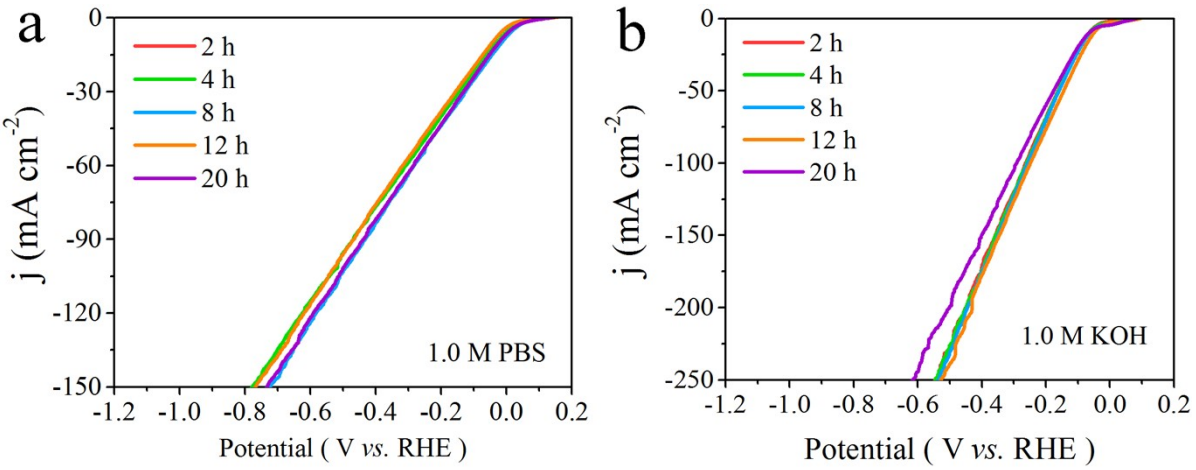

Fig. S10. LSV curves (without *iR* compensation) of Ru/Nb_2O_5 with different soaking times in (a) 1.0 M PBS and (b) 1.0 M KOH.

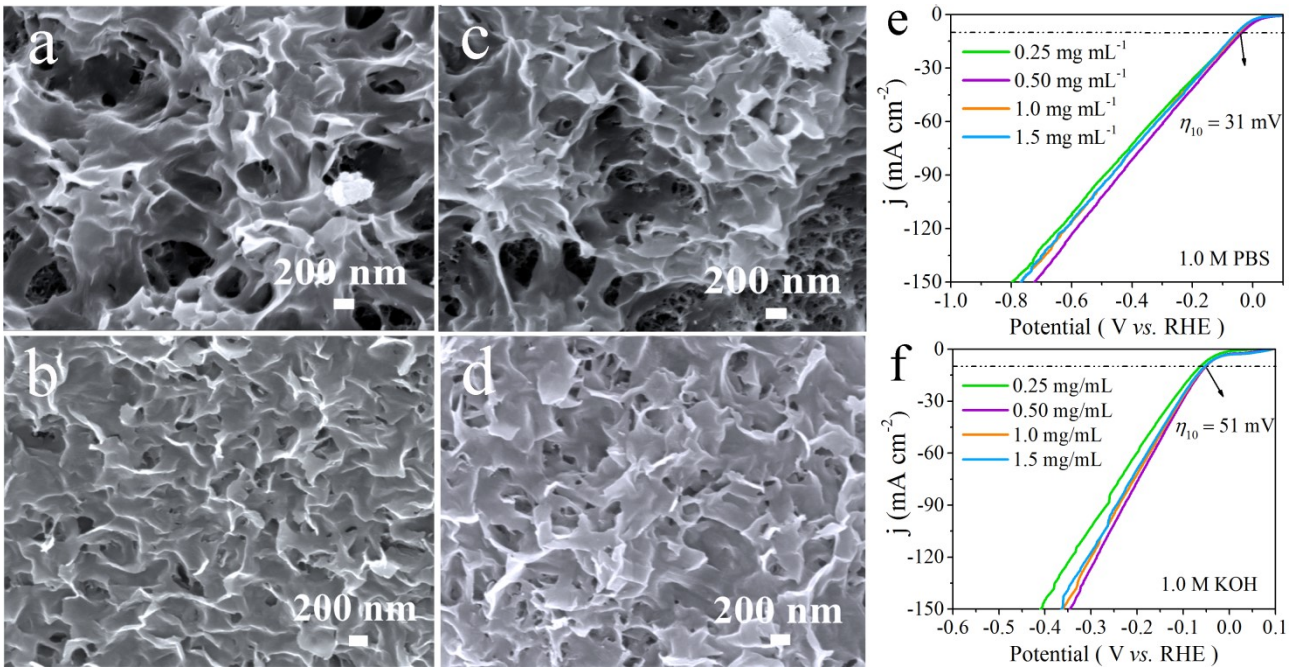

Fig. S11. SEM images of Ru/Nb_2O_5 obtained using different concentrations of $RuCl_3 \cdot xH_2O$: (a) 0.25, (b) 0.50, (c) 1.0, and (d) 1.5 mg mL^{-1}. LSV curves (without *iR* compensation) of Ru/Nb_2O_5 obtained using different concentrations of $RuCl_3 \cdot xH_2O$ in (e) 1.0 M PBS and (f) 1.0 M KOH. The volume of the solution was controlled at 4.0 mL during the experiment.

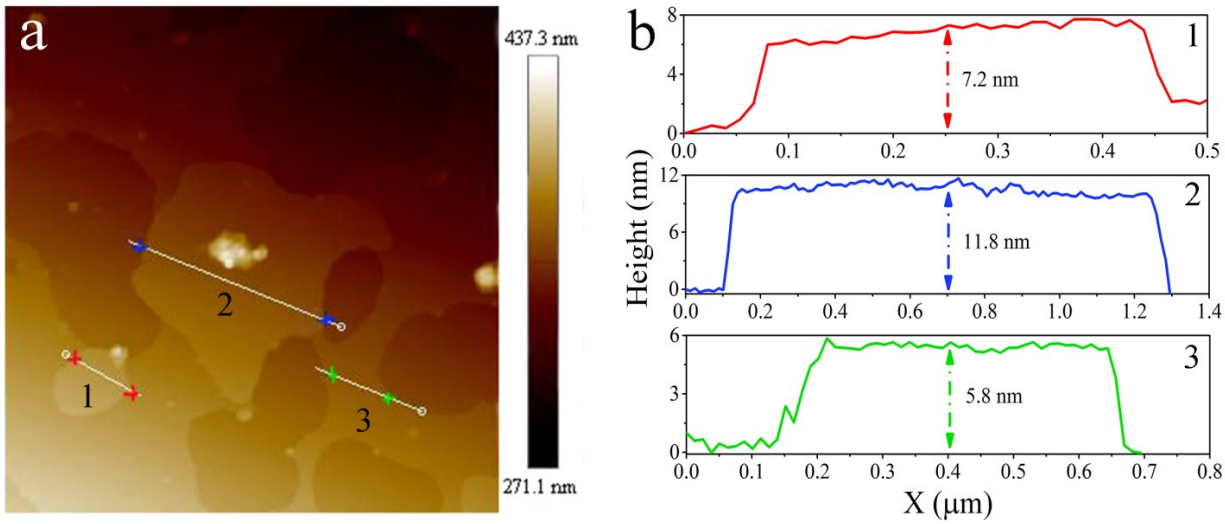

Fig. S12. (a) AFM image of Ru/Nb_2O_5 and (b) the corresponding height curve.

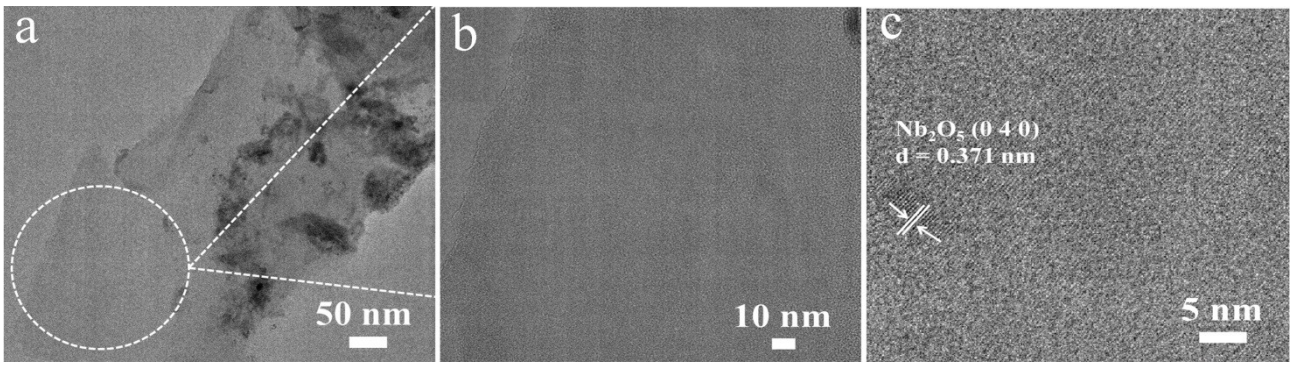

Fig. S13. (a, b) TEM and (c) HRTEM images of pure Nb_2O_5.

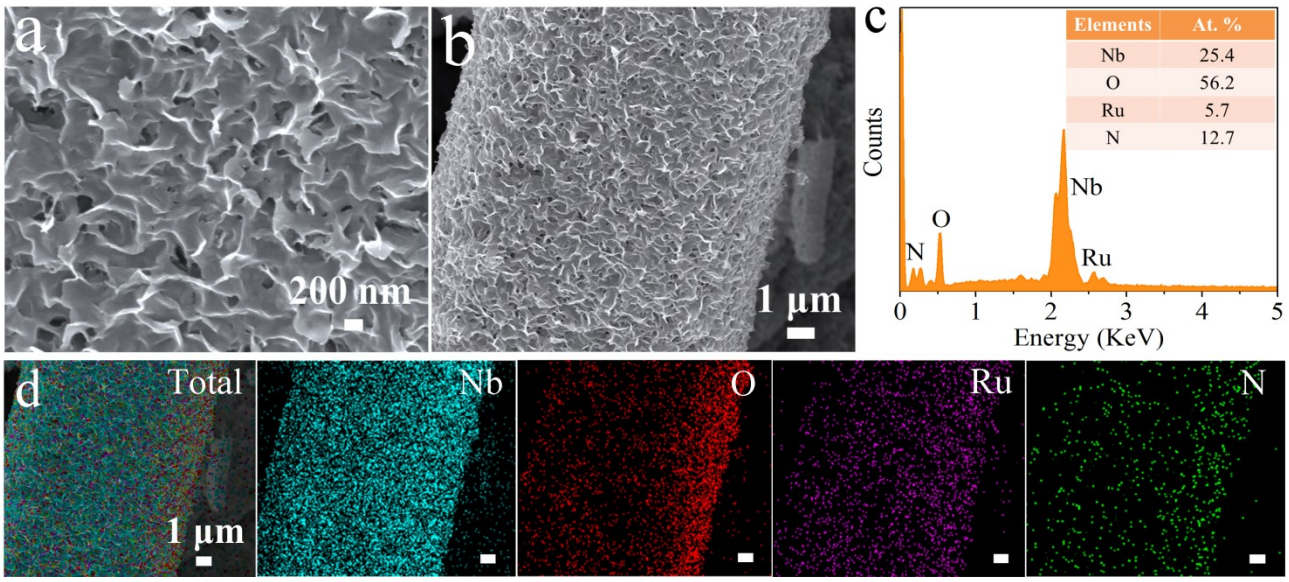

Fig. S14. (a, b) SEM images, (c) EDS data, and (d) elemental mapping diagrams of Ru/Nb_2O_5.

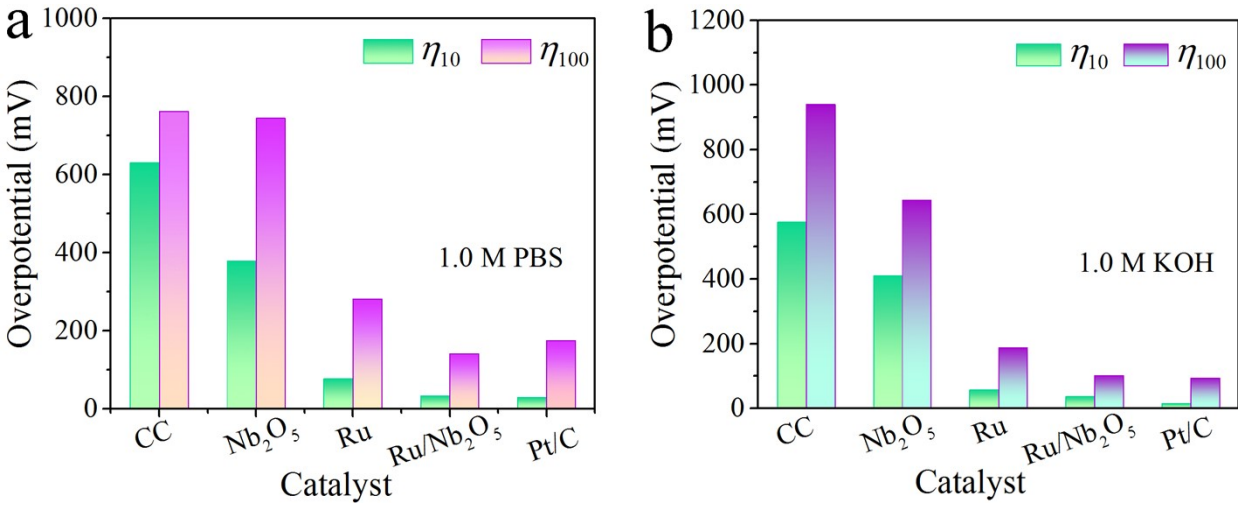

Fig. S15. Comparison of η_{10} and η_{100} for CC, Nb_2O_5, Ru, Ru/Nb_2O_5, and Pt/C in (a) 1.0 M PBS and (b) 1.0 M KOH.

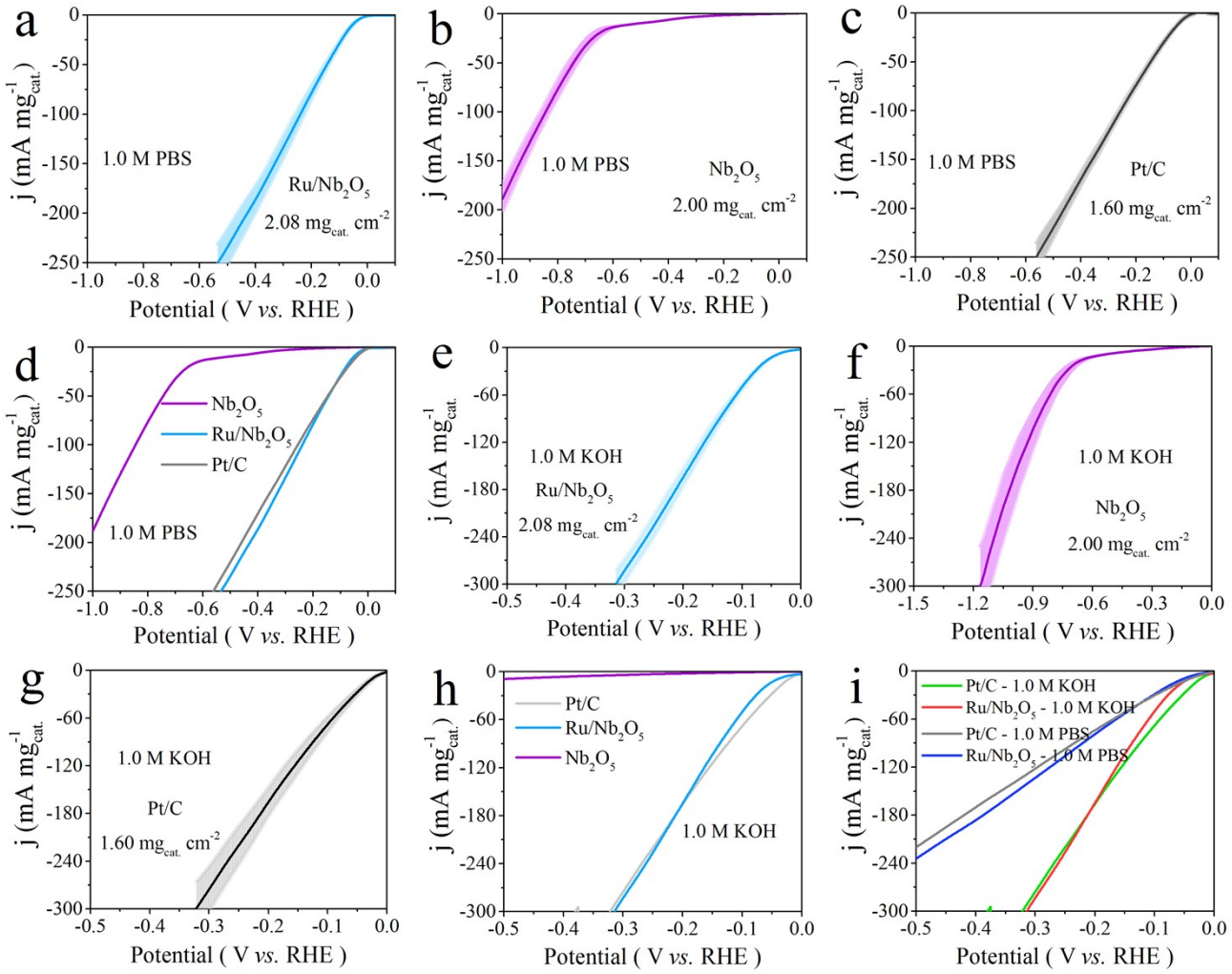

Fig. S16. *IR*-corrected LSV curves of (a) Ru/Nb_2O_5, (b) Nb_2O_5, and (c) Pt/C normalized by mass loading of catalyst, (d) the average j_m^c of the above catalysts in 1.0 M PBS. *IR*-corrected LSV curves of (e) Ru/Nb_2O_5, (f) Nb_2O_5, and (g) Pt/C normalized by mass loading of catalyst, (h) the average j_m^c of the above catalysts in 1.0 M KOH. (i) Comparison of the j_m^c of Ru/Nb_2O_5 and Pt/C under neutral and alkaline conditions. To analyze statistical errors, five parallel measurements were conducted for five identical catalysts, and the data highlighted represents the average of all 5 measurements.

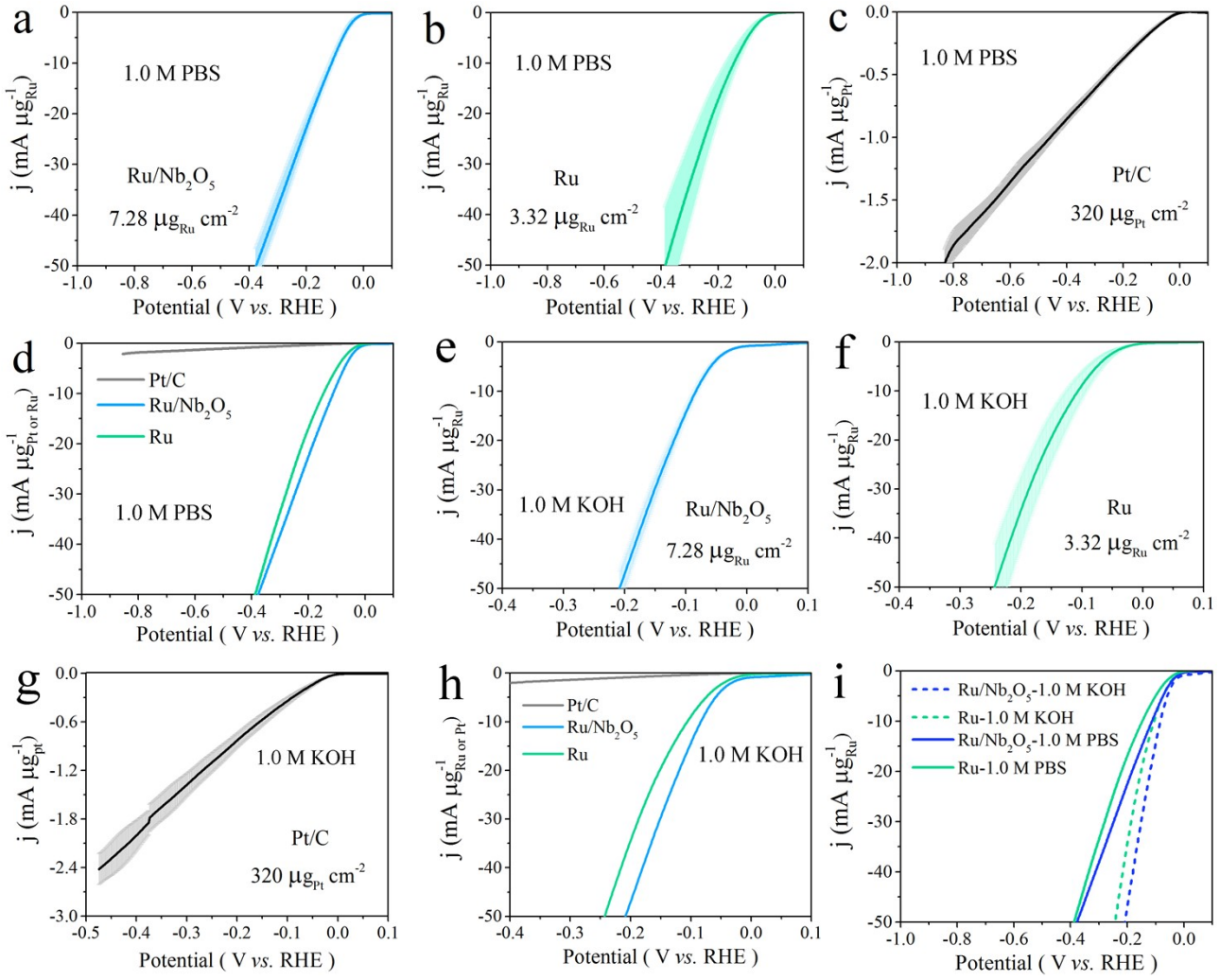

Fig. S17. *IR*-corrected LSV curves of (a) Ru/Nb_2O_5, (b) Ru, and (c) Pt/C normalized by mass loading of Ru or Pt, (d) the average j_m of the above catalysts in 1.0 M PBS. *IR*-corrected LSV curves of (e) Ru/Nb_2O_5, (f) Ru, and (g) Pt/C normalized by mass loading of Ru or Pt, (h) the average j_m of the above catalysts in 1.0 M KOH. (i) Comparison of the j_m of Ru/Nb_2O_5 and Ru under neutral and alkaline conditions. To analyze statistical errors, five parallel measurements were conducted for five identical catalysts, and the data highlighted represents the average of all 5 measurements.

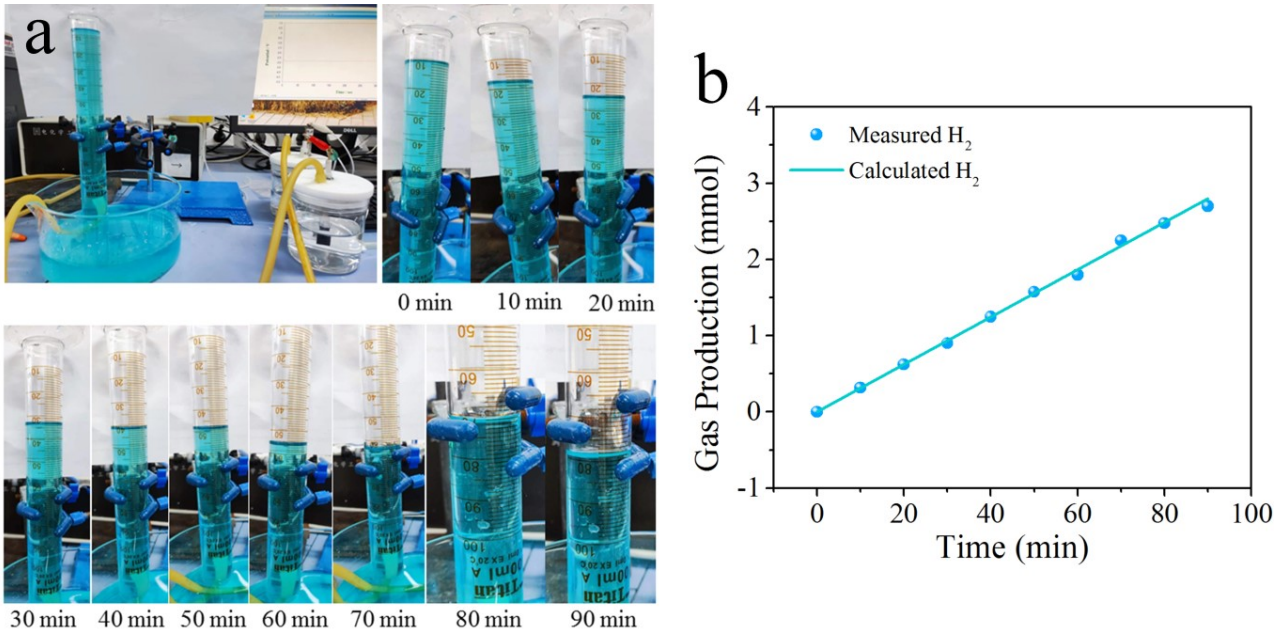

Fig. S18. (a) The device used to collect H_2 and the volume of H_2 produced at different times (the current density is -100 mA cm^{-2}). (b) Theoretical and experimental comparison of the produced H_2 amount of Ru/Nb_2O_5 in HER process.

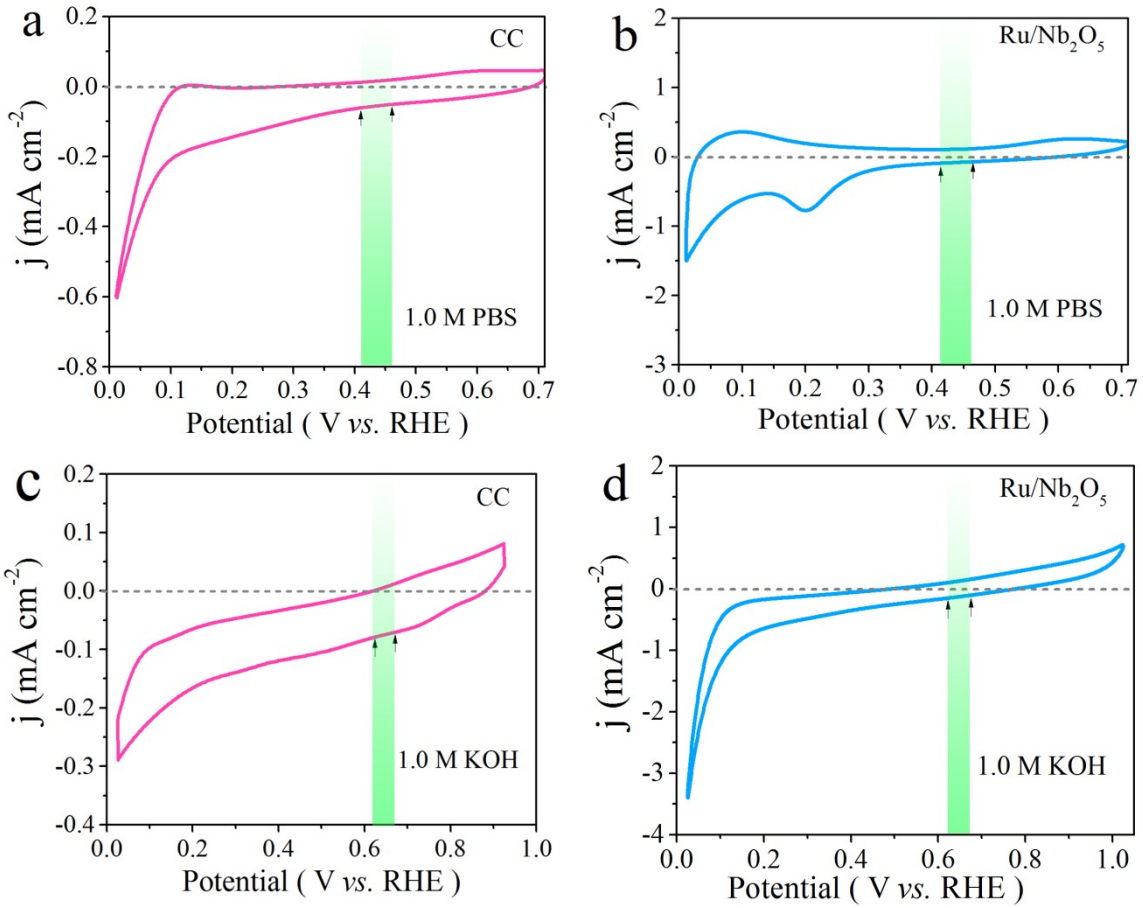

Fig. S19. The CV curves of (a) bare CC and (b) Ru/Nb_2O_5 measured in Ar-saturated 1.0 M PBS in the potential range of 0.0 - 0.7 V *vs.* RHE. The CV curves of (c) bare CC and (d) Ru/Nb_2O_5 measured in Ar-saturated 1.0 M KOH in the potential range of 0.0 - 1.0 V *vs.* RHE. The scan rate is 20 mV s^{-1}.

During the testing process, we continuously introduced Ar into the electrolyte (1.0 M PBS and 1.0 M KOH) to eliminate the influence of O_2 reduction reactions on the experimental results. Before analyzing the double-layer capacitance (C_{dl}), cyclic voltammetry tests were conducted in the potential ranges of 0.0 - 0.7 V *vs.* RHE (1.0 M PBS) and 0.0 - 1.0 V *vs.* RHE (1.0 M KOH) to determine suitable regions. As depicted in Fig. S19, due to the oxidation-reduction characteristics and capacitance properties of CC[15, 16] and Ru/Nb_2O_5,[11, 17] finding regions with completely

symmetric cathodic and anodic currents in both electrolytes is a challenge. For Ru/Nb_2O_5, the potential ranges of 0.411 - 0.461 V *vs.* RHE (1.0 M PBS) and 0.625 - 0.675 V *vs.* RHE (1.0 M KOH) were closer to the non-faradaic region; therefore, these two ranges were selected for electrochemical capacitance testing. Given the significant differences in electrochemical behavior among different materials, our approach is to choose the same testing regions based on the Ru/Nb_2O_5 as a reference, which is also a method adopted in many current studies.[18, 19]

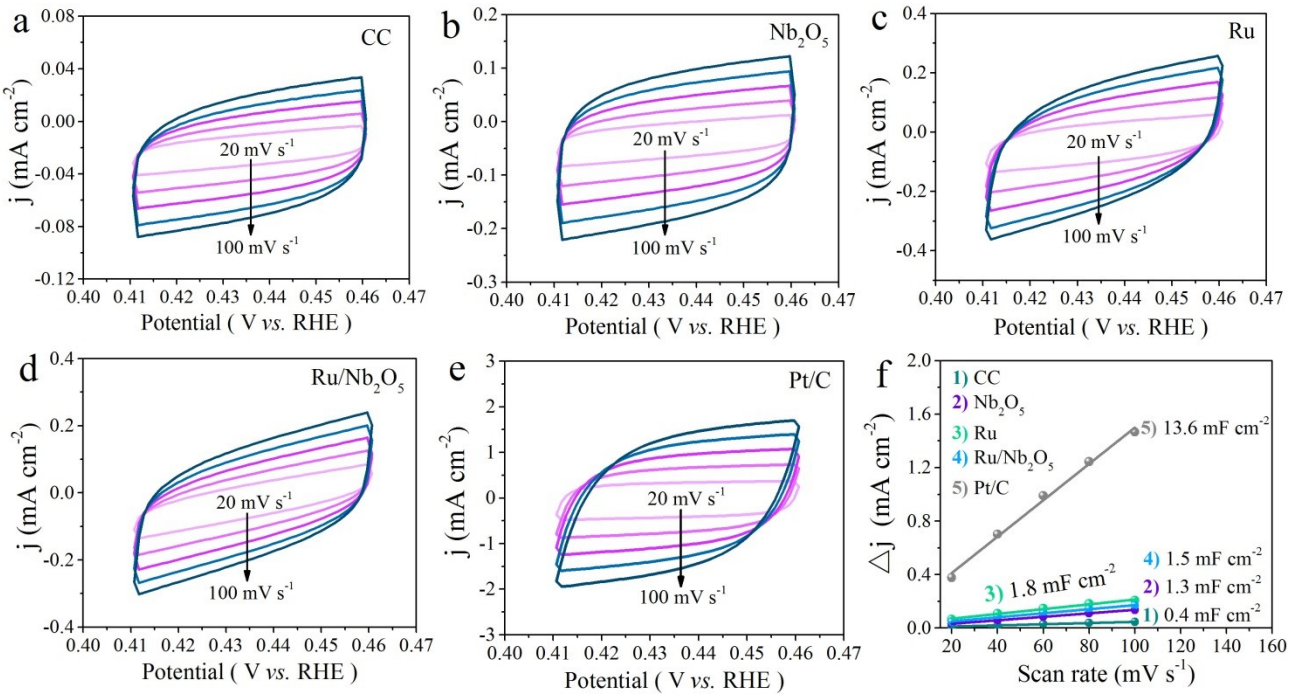

Fig. S20. CV curves of (a) CC, (b) Nb_2O_5, (c) Ru, (d) Ru/Nb_2O_5, and (e) Pt/C measured in 1.0 M PBS at scan rates of 20 to 100 mV s^{-1}. (f) The capacitive current at 0.436 V *vs.* RHE of the as-prepared catalysts.

The electrochemically active surface area (ECSA) was estimated by measuring the electrochemical double-layer capacitance (C_{dl}). To estimate the C_{dl} in 1.0 M PBS, cyclic voltammetry (CV) was carried out in the non-faradaic potential region of 0.411 to 0.461 V *vs*. RHE with various scan rates of 20, 40, 60, 80, and 100 mV s^{-1}, respectively, and then the capacitive current $\Delta j = (j_a - j_c)/2$ at 0.436 V *vs*. RHE was plotted versus the scan rate. The ECSA was calculated by ECSA = C_{dl}/C_s, where C_s is the specific capacitance using an average value of 0.040 mF cm^{-2}. The ECSA of CC, Nb_2O_5, Ru, Ru/Nb_2O_5, and Pt/C are 10.0, 32.5, 45.0, 37.5, and 340 cm^2, respectively.

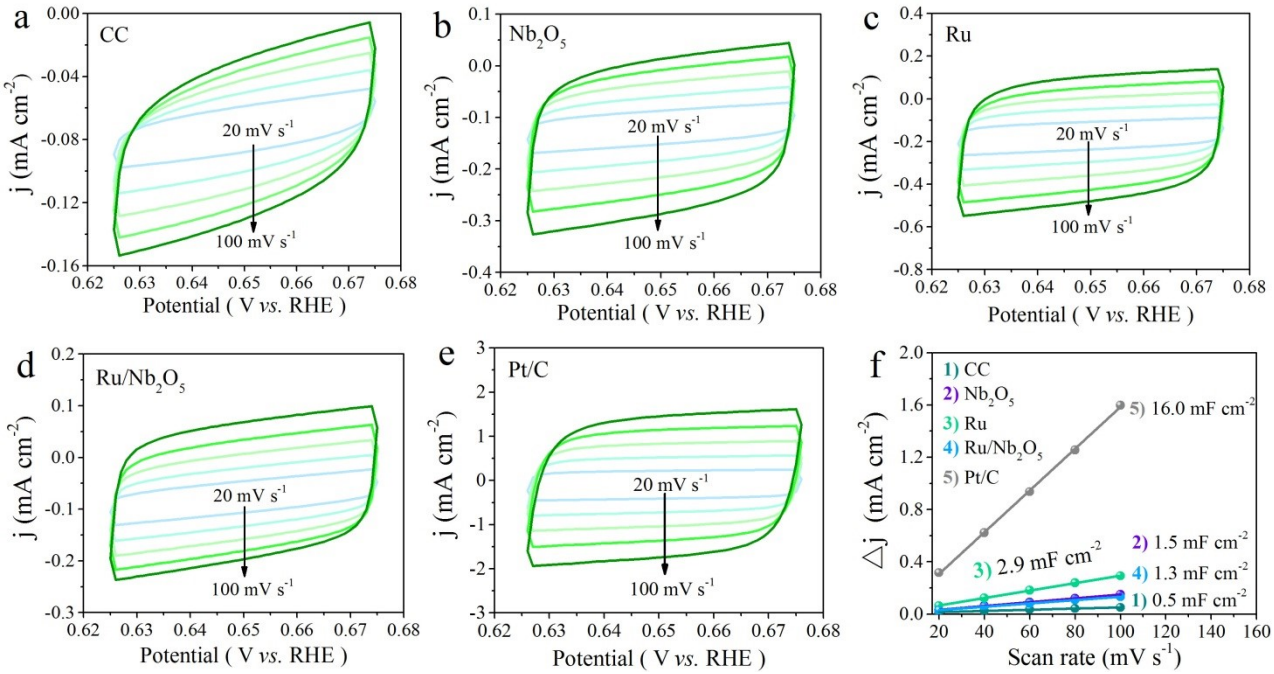

Fig. S21. CV curves of (a) CC, (b) Nb_2O_5, (c) Ru, (d) Ru/Nb_2O_5, and (e) Pt/C measured in 1.0 M KOH at scan rates of 20 to 100 mV s^{-1}. (f) The capacitive current at 0.650 V *vs.* RHE of the as-prepared catalysts.

To estimate the C_{dl} in 1.0 M KOH, CV was carried out in the non-faradaic potential region of 0.625 to 0.675 V *vs*. RHE with various scan rates of 20, 40, 60, 80, and 100 mV s^{-1}, respectively, and then the capacitive current $\Delta j = (j_a - j_c)/2$ at 0.650 V *vs*. RHE was plotted versus the scan rate. The ECSA was calculated by ECSA = C_{dl}/C_s, where C_s is the specific capacitance using an average value of 0.040 mF cm^{-2}. The ECSA of CC, Nb_2O_5, Ru, Ru/Nb_2O_5, and Pt/C are 12.5, 37.5, 72.5, 32.5, and 400 cm^2, respectively.

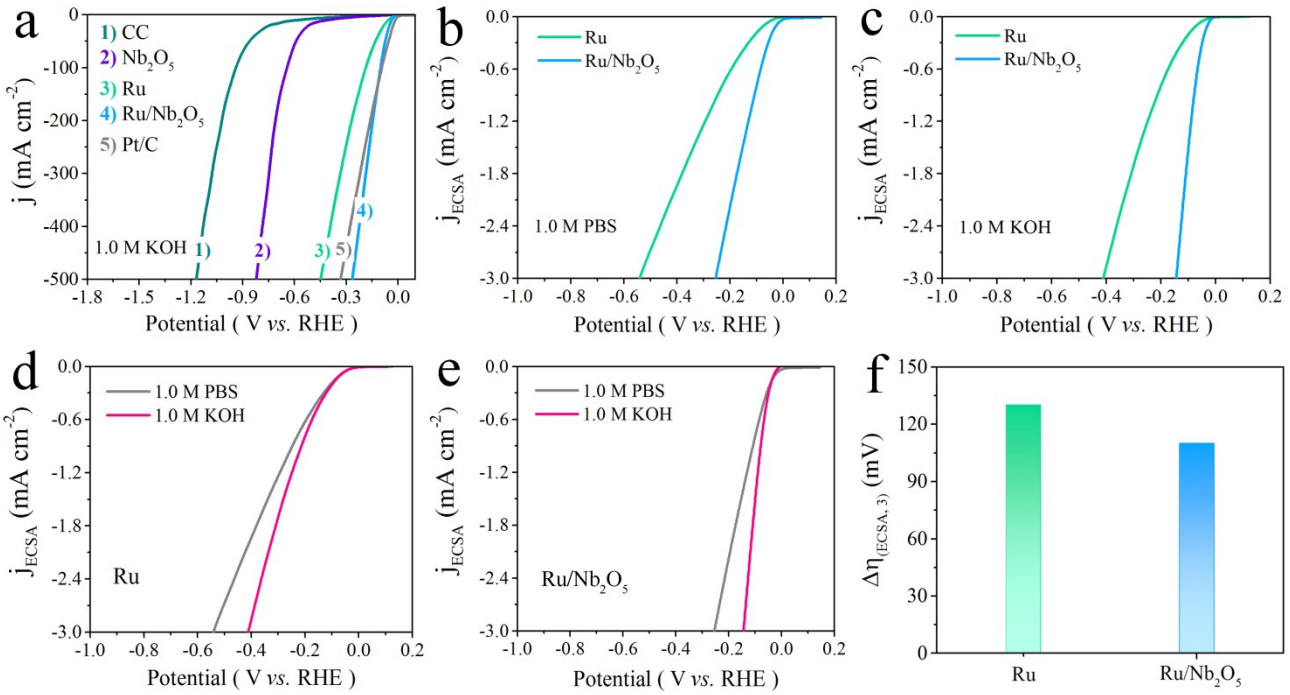

Fig. S22. (a) LSV curves of the as-prepared catalysts in 1.0 M KOH. Comparison of ECSA normalized LSV curves of Ru and Ru/Nb_2O_5 in (b) 1.0 M PBS and (c) 1.0 M KOH. Comparison of ECSA normalized LSV curves of (d) Ru and (e) Ru/Nb_2O_5 in alkaline and neutral electrolytes. (f) η difference between the alkaline and neutral electrolyte at j_{ECSA} = -3 mA cm^{-2} for Ru and Ru/Nb_2O_5.

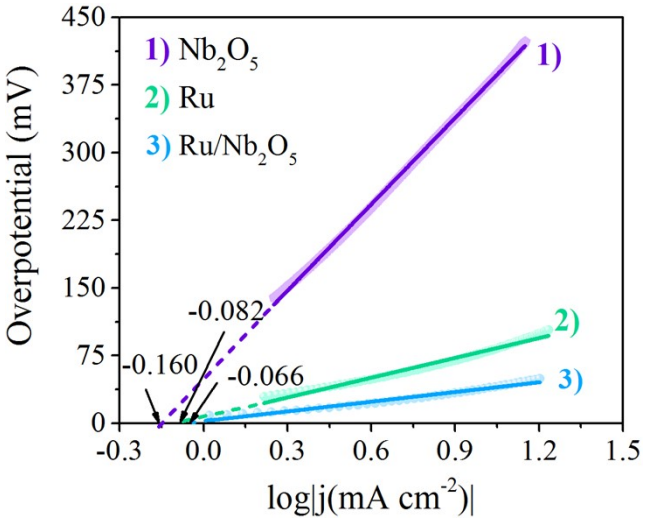

Fig. S23. Exchange current density (j_0) of Nb_2O_5, Ru, and Ru/Nb_2O_5. The j_0 of Nb_2O_5, Ru, and Ru/Nb_2O_5 are 0.692, 0.828, and 0.859 mA cm^{-2}, respectively.

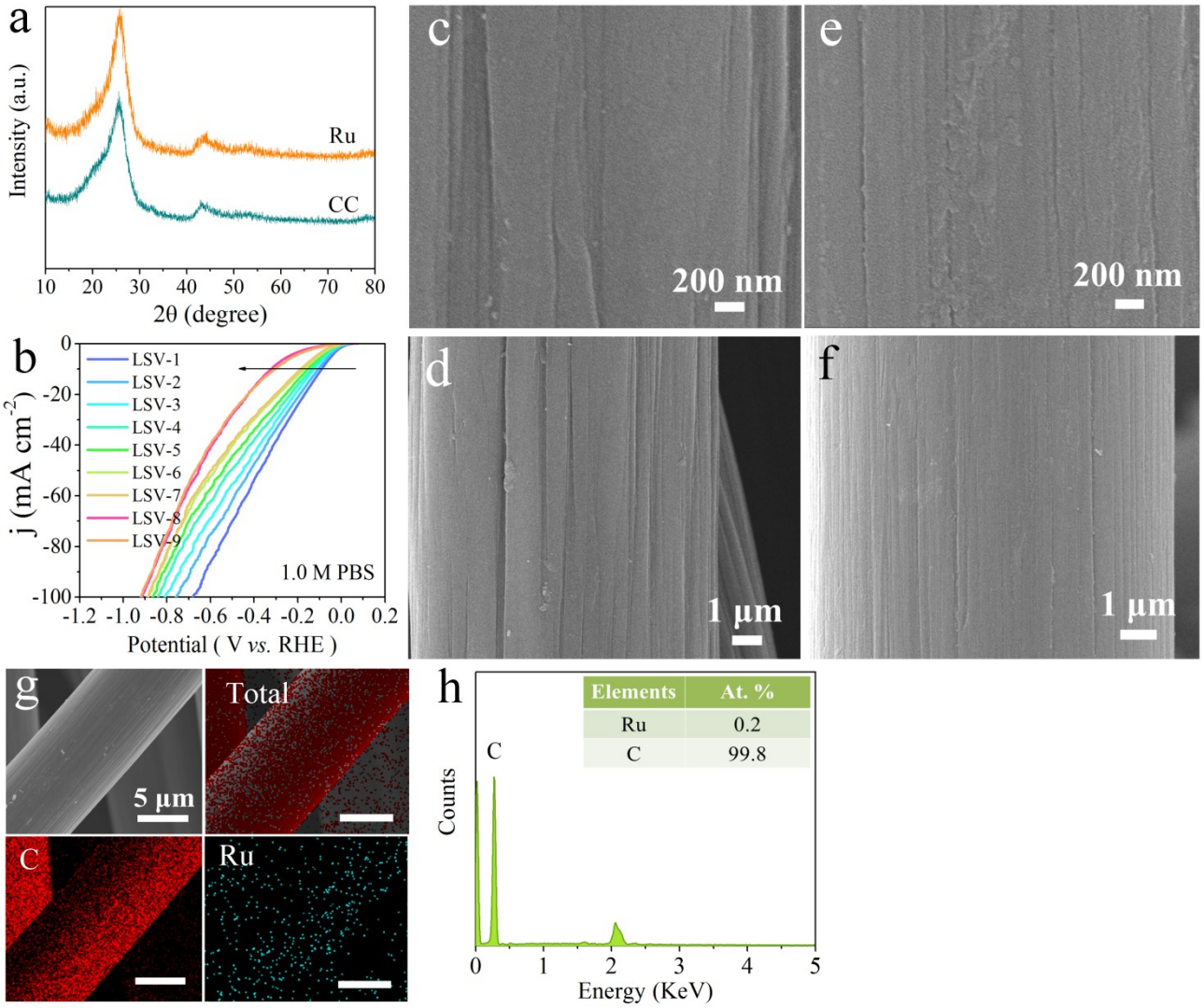

Fig. S24. (a) XRD patterns of bare CC and Ru, (b) LSV curves (without *iR* compensation) of Ru in 1.0 M PBS, where the number on the curve represents the number of scans. SEM images of (c, d) bare CC and (e, f) Ru. (g) Elemental mapping diagrams and (h) EDS data of Ru.

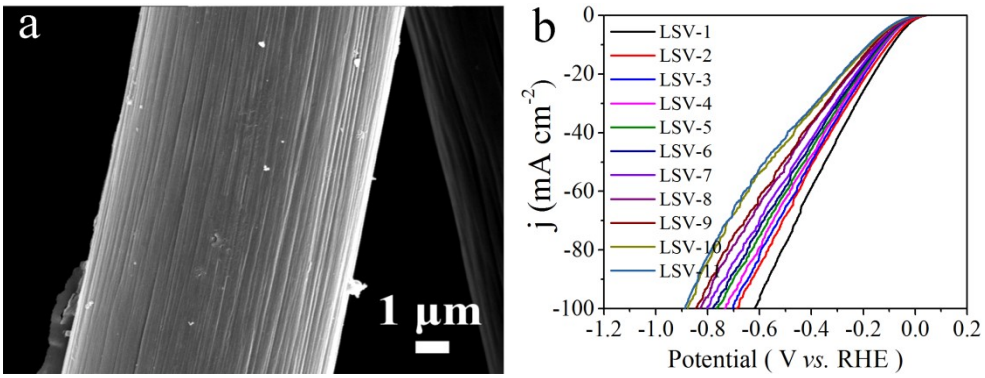

Fig. S25. (a) The SEM image and (b) LSV curves (without *iR* compensation) tested in 1.0 M PBS of H-Ru, where the number on the curve represents the number of scans.

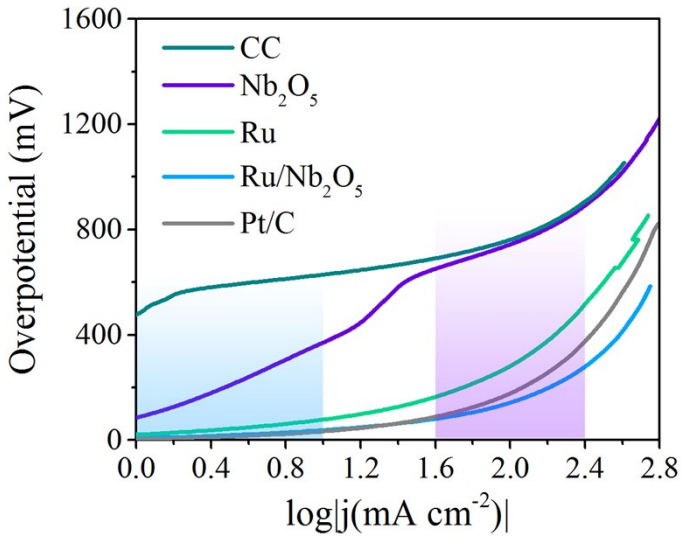

Fig. S26. The total Tafel plots of CC, Nb_2O_5, Ru, Ru/Nb_2O_5, and Pt/C.

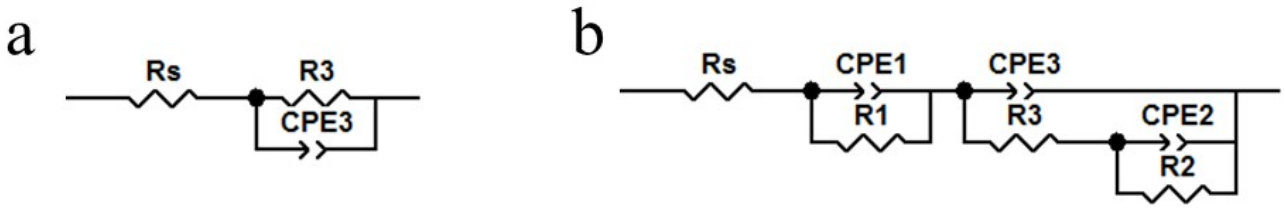

Fig. S27. The equivalent circuit models of (a) Ru and (b) Ru/Nb_2O_5.

Ru only shows one semicircle in the mid-frequency region (10 - 100 Hz), corresponding to R_3||CPE_3.[20, 21] Fig. S27b shows the equivalent circuit diagram for Ru/Nb_2O_5, where the resistance for electron transport through the Nb_2O_5 layer (R_1||CPE_1) is located in the high-frequency region, the charge transfer resistance (R_3||CPE_3) is located in the mid-frequency region, and the H^* accumulation (R_2||CPE_2) is located in the low-frequency region.[22, 23] Based on the Nyquist and Bode plots of Ru and Ru/Nb_2O_5, we have drawn the corresponding equivalent circuits.

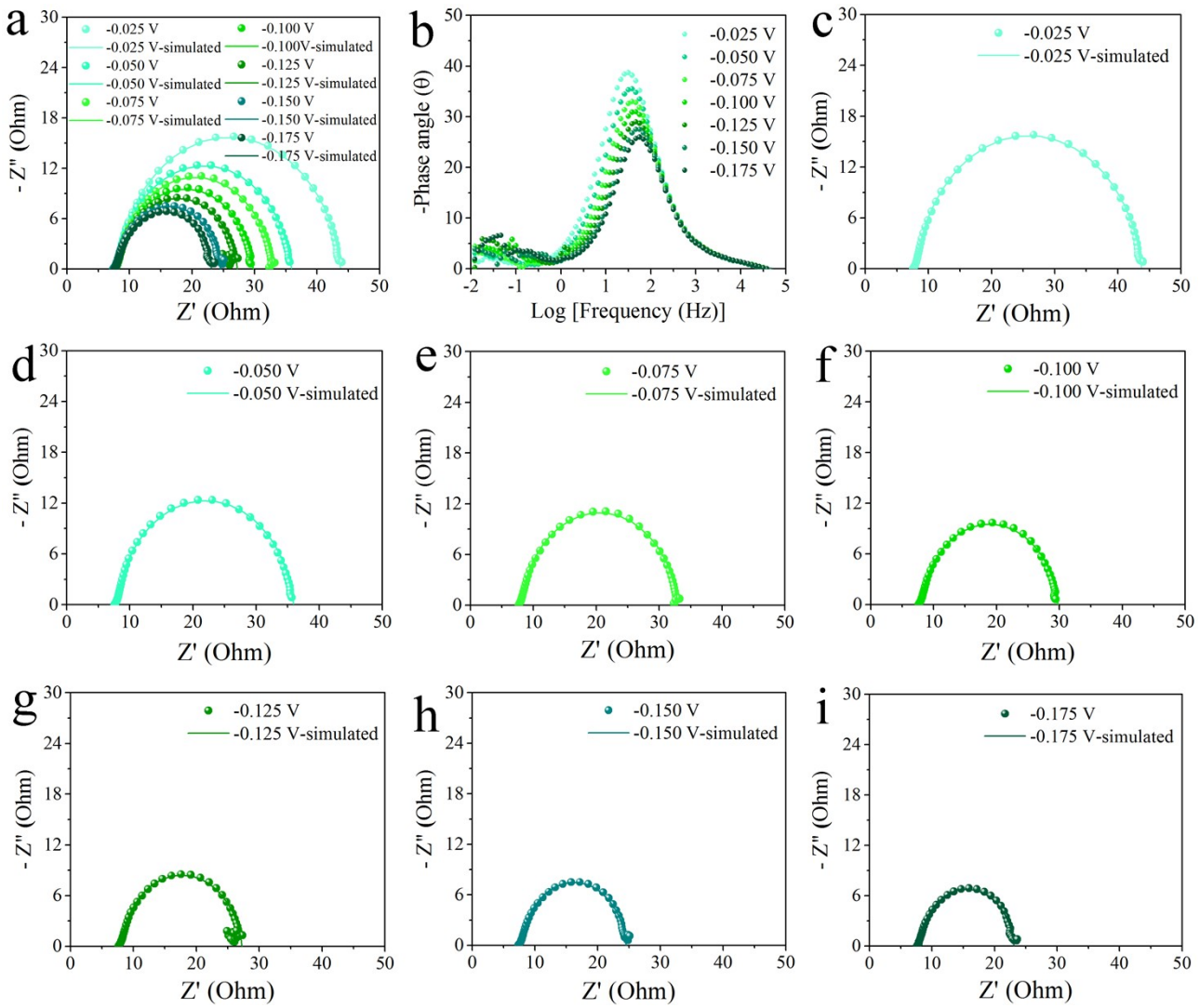

Fig. S28. (a) Nyquist and (b) Bode plots of Ru at different potentials. Experimental (circled points) and simulated (solid lines) Nyquist plots for Ru at potentials of (c) -0.025 V, (d) -0.050 V, (e) -0.075 V, (f) -0.100 V, (g) -0.125 V, (h) -0.150 V, and (i) -0.175 V.

As shown in Fig. S28, the Nyquist curves of Ru were fitted according to its equivalent circuit model, and the experimental values match well with the simulated ones. In this electrochemical system, the solution resistance (R_s) is approximately 8 Ω. When the overpotential increases from -0.025 V to -0.175 V, R_3 decreases from 35.70 to 15.17 Ω (Table S6).

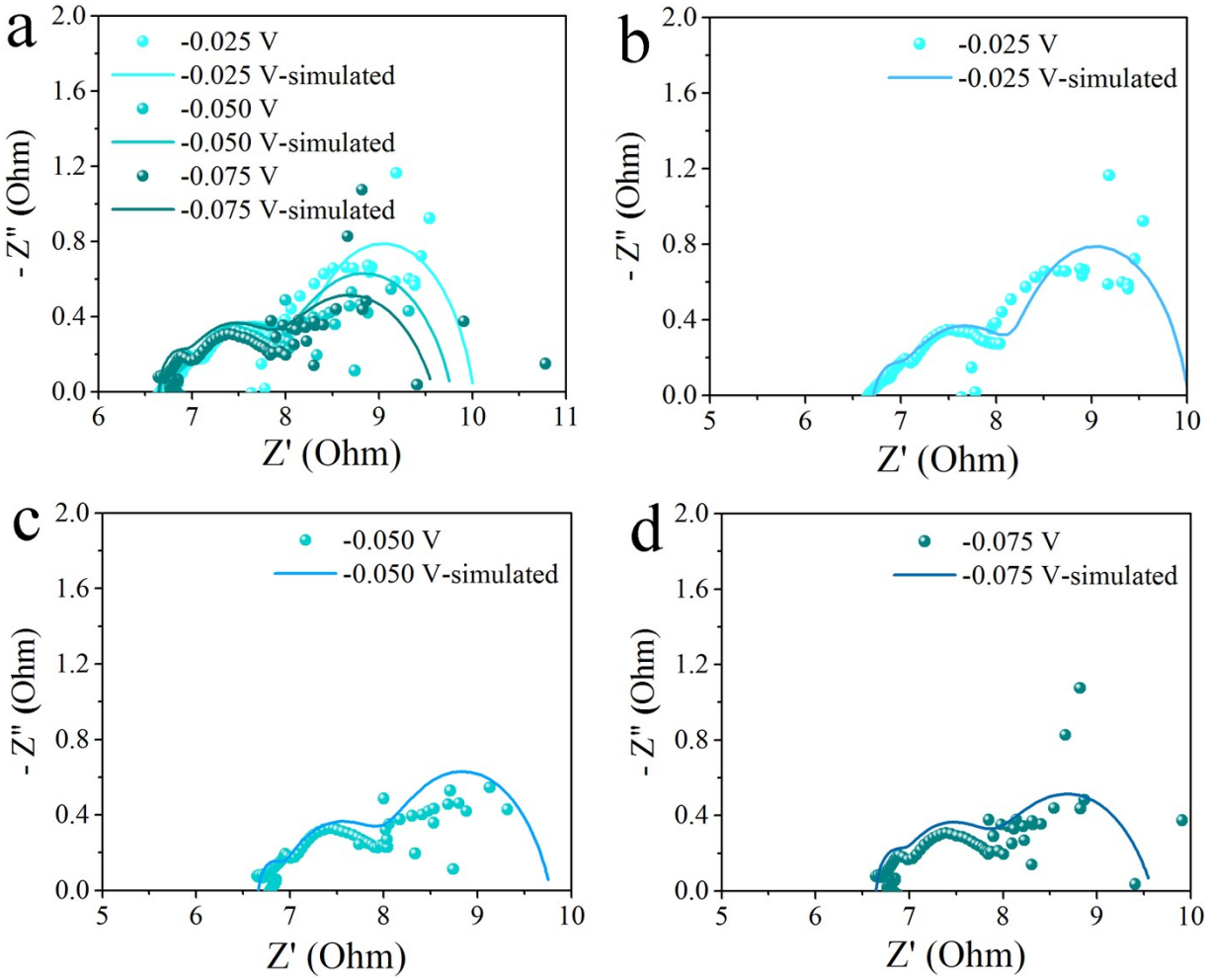

Fig. S29. (a) Nyquist plots of Ru/Nb_2O_5 at different potentials. Experimental (circled points) and simulated (solid lines) Nyquist plots for Ru/Nb_2O_5 at potentials of (b) -0.025 V, (c) -0.050 V, and (d) -0.075 V.

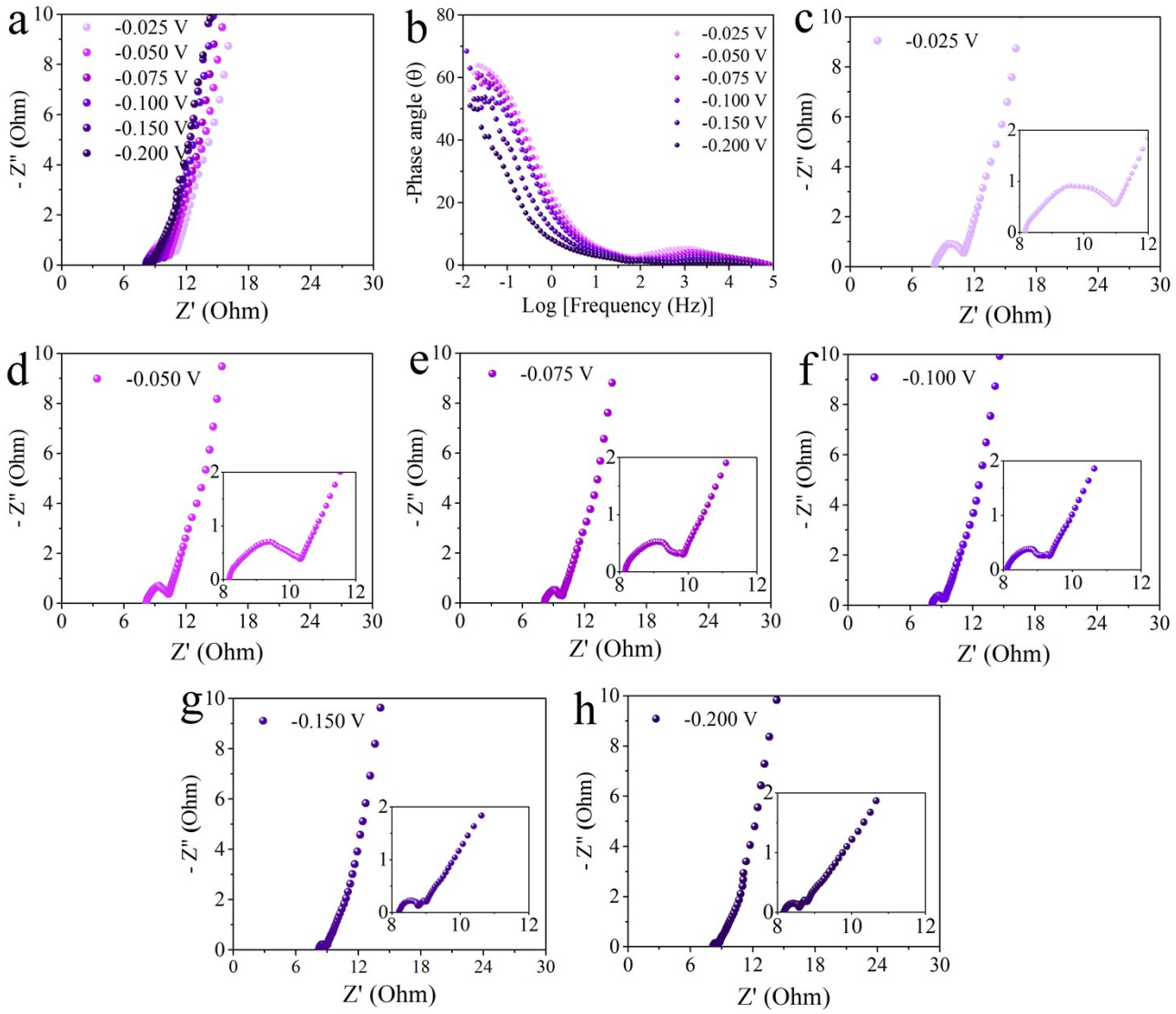

Fig. S30. (a) Nyquist and (b) Bode plots of Nb_2O_5 at different potentials. Experimental Nyquist plots for Nb_2O_5 at potentials of (c) -0.025 V, (d) -0.050 V, (e) -0.075 V, (f) -0.100 V, (g) -0.150 V, and (h) -0.200 V.

As shown in Fig. S30, the Nyquist curves of Nb_2O_5 consist of a semicircle and a sloping line. In this electrochemical system, the solution resistance (R_s) is approximately 8 Ω.

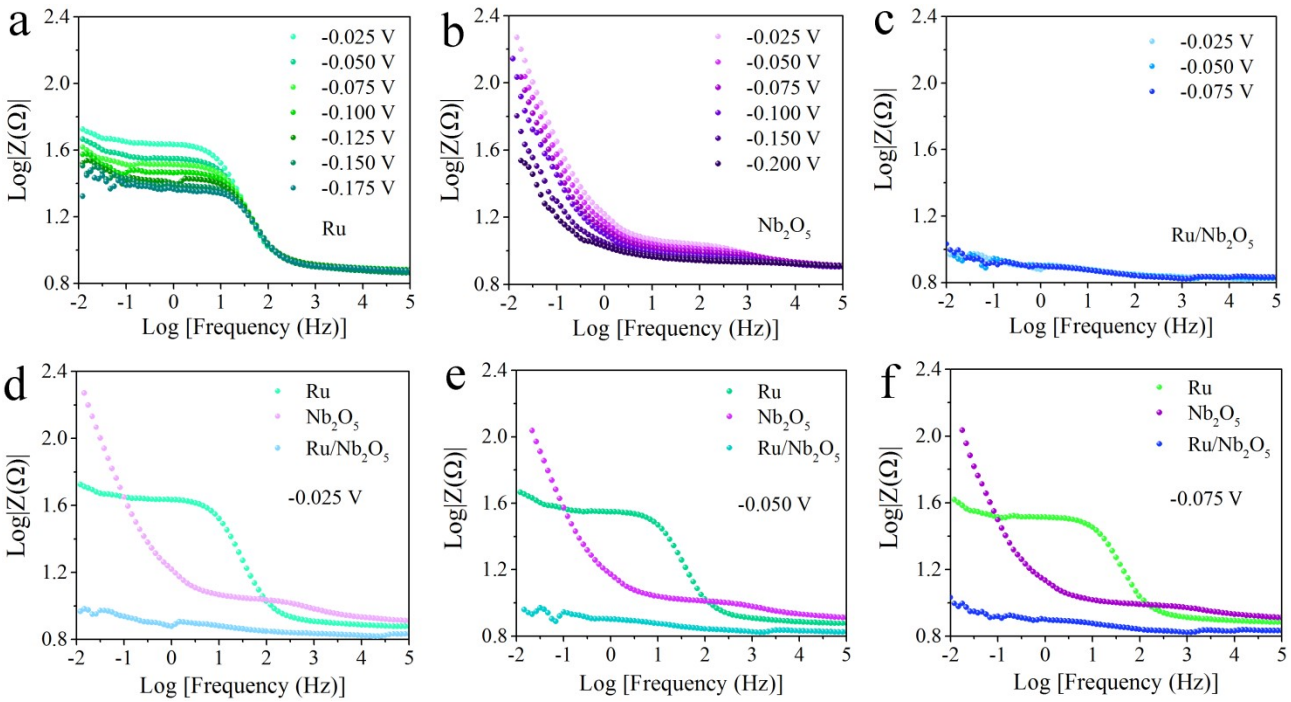

Fig. S31. Bode amplitude plots of (a) Ru, (b) Nb_2O_5, and (c) Ru/Nb_2O_5 at different overpotentials. Comparison of Bode amplitude plots for Ru, Nb_2O_5, and Ru/Nb_2O_5 at (d) -0.025 V, (e) -0.050 V, and (f) -0.075 V.

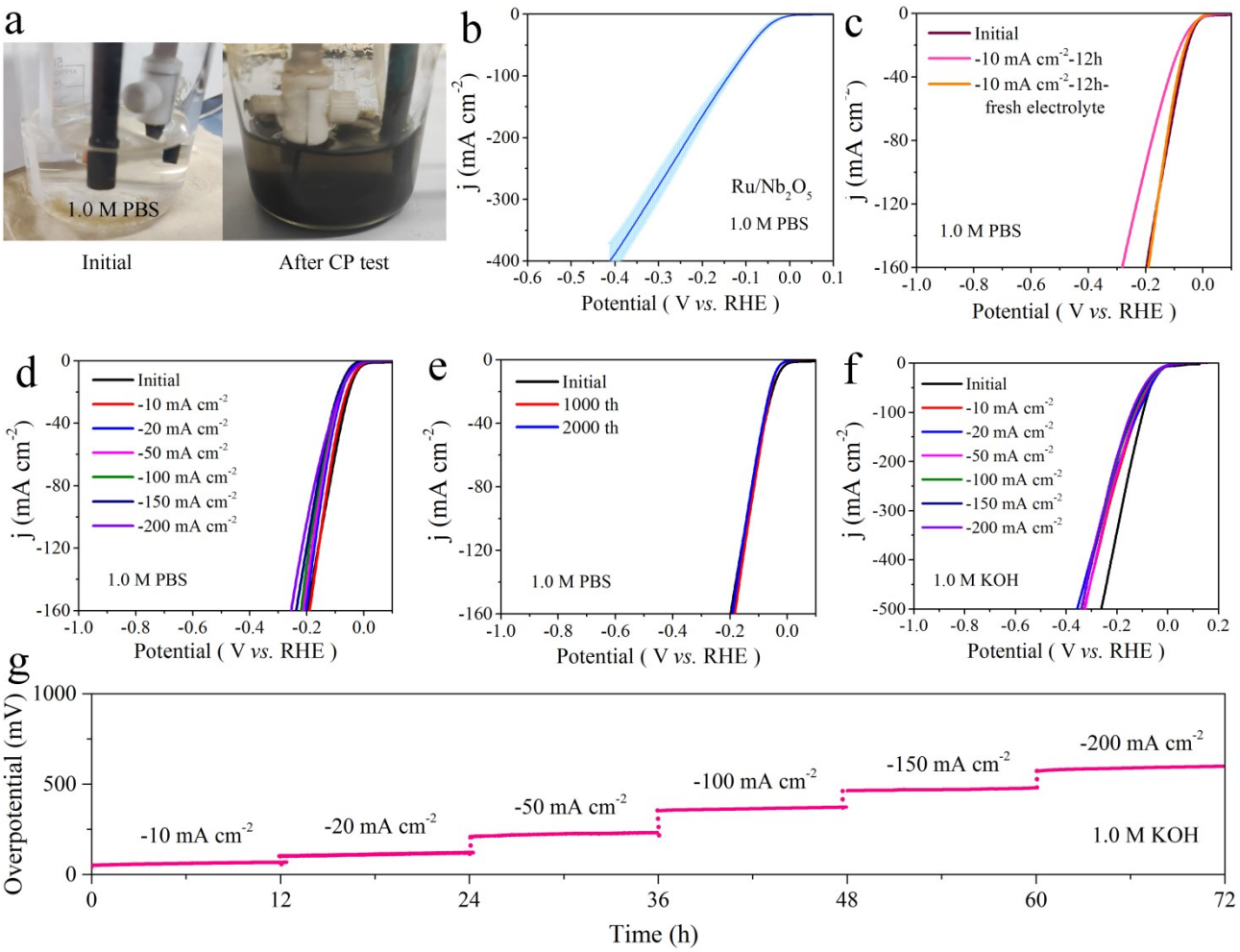

Fig. S32. (a) The changes in the electrolyte before and after testing at -10 mA cm^{-2} for 12 hours, (b) LSV curves of 5 different Ru/Nb_2O_5, the data highlighted in blue represents the average of all 5 measurements, (c) the polarization curves of Ru/Nb_2O_5 in fresh (orange and black line) and contaminated (pink line) 1.0 M PBS. (d) LSV curves of Ru/Nb_2O_5 obtained by maintaining the current densities at -10, -20, -50, -100, -150, and -200 mA cm^{-2} for 12 h in 1.0 M PBS. (e) LSV curves of Ru/Nb_2O_5 before and after 1000/2000 CV cycles (potential window without *iR*-compensation for CV: 0.211 - -0.989 V *vs.* RHE, scan rate: 100 mV S^{-1}). (f) LSV curves of Ru/Nb_2O_5 obtained by maintaining the current densities at -10, -20, -50, -100, -150, and -200 mA cm^{-2} for 12 h in 1.0 M KOH. Note: Without specific instructions, LSV curves are recorded in fresh electrolyte. (g) The multistep CP curves of Ru/Nb_2O_5 at different current densities in 1.0 M KOH.

As shown in Fig. S32a, the electrolyte before and after continuous testing for approximately 12 hours at -10 mA cm^{-2} is depicted. During the multistep CP testing, the graphite rod serving as the counter electrode experienced dissolution, releasing carbon particles and CO into the solution, causing the 1.0 M PBS to turn black. These carbon particles and CO adsorbed onto the Ru/Nb_2O_5 surface, leading to a decrease in activity. It is noteworthy that LSV curves recorded in the contaminated solution also revealed noticeable activity decay, but that there were no significant differences from the initial activity observed by LSV after a fresh electrolyte was used (Fig. S32c). After conducting stability tests at each current density, the *iR*-compensated LSV curves in clean electrolyte also show no significant activity decay (Fig. S32d).

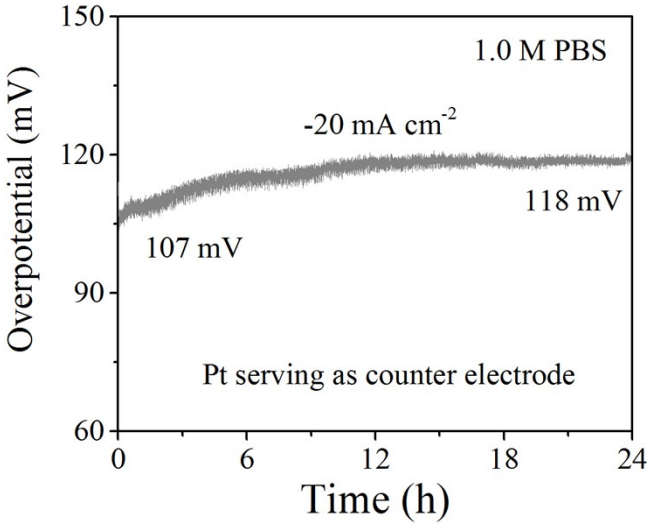

Fig. S33. The CP curve of Ru/Nb_2O_5 recorded employing a Pt counter electrode in 1.0 M PBS.

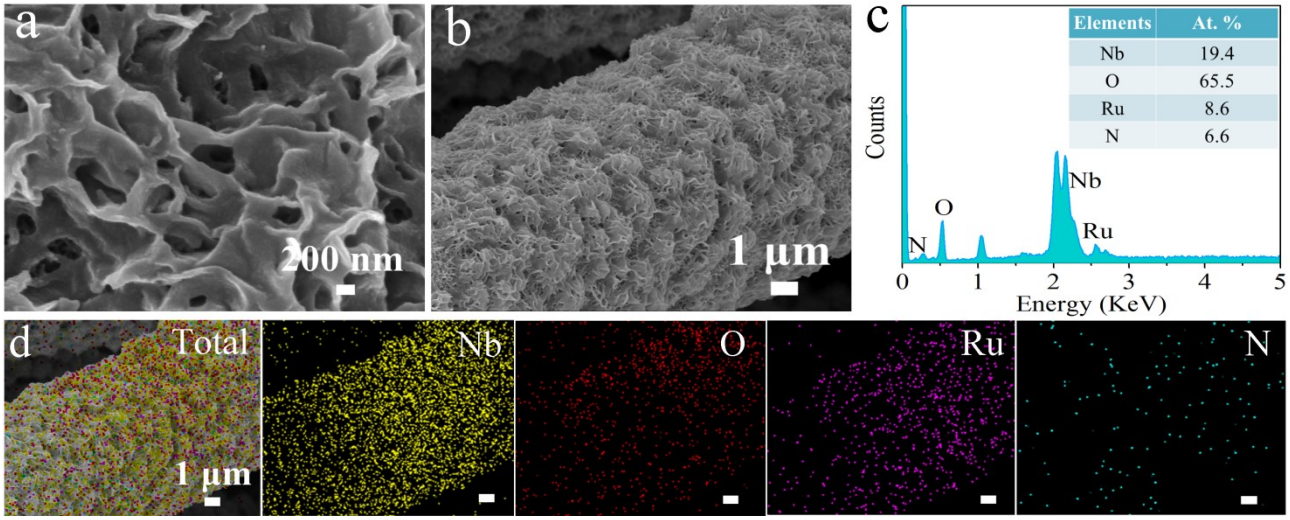

Fig. S34. (a, b) SEM images, (c) EDS data, and (d) elemental mapping diagrams of Ru/Nb_2O_5 after the CP test.

After long-term stability tests at different current densities (-10, -20, -50, -100, -150, and -200 mA cm^{-2}), the content of Nb decreased to 19.4%, while the content of Ru increased to 8.6 At.%. The Nb_2O_5 serving as the carrier partially dissolved in the electrolyte, resulting in a decrease in the content of Nb. Relatively, the content of Ru increased.

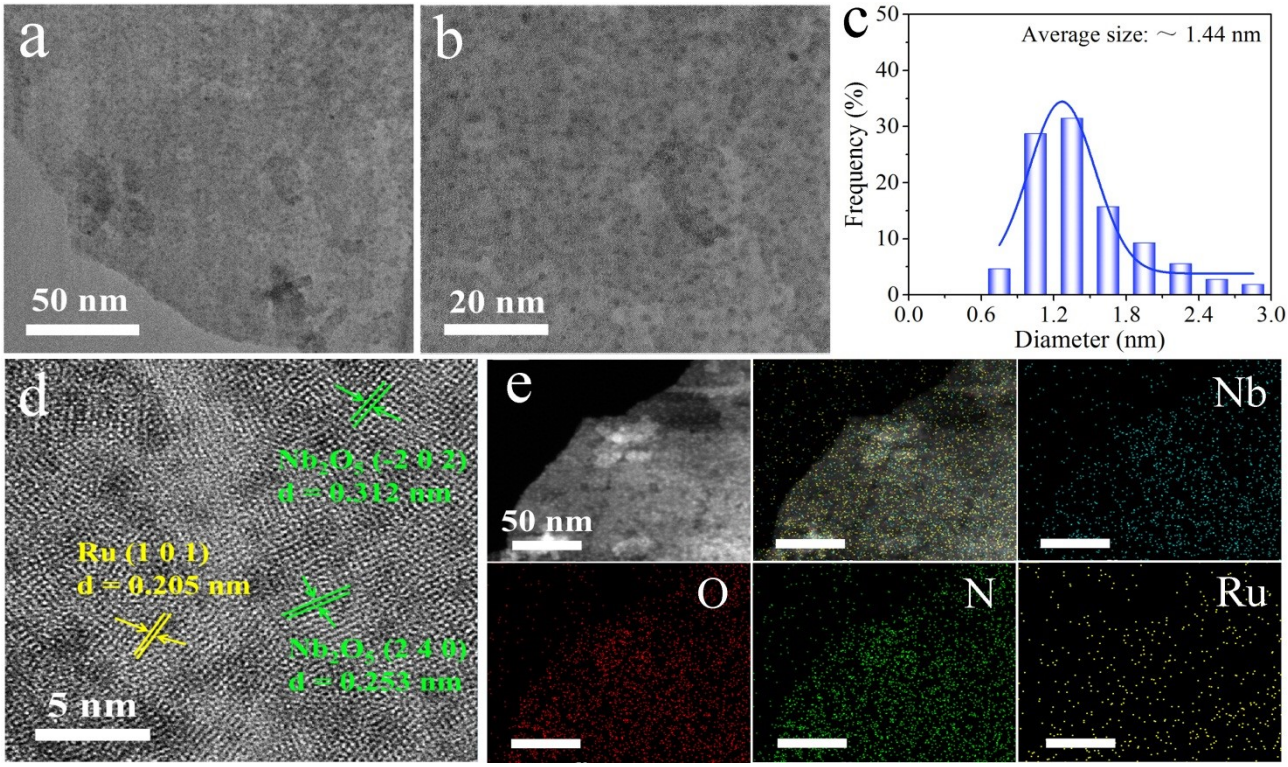

Fig. S35. (a, b) TEM, (c) particle size statistics of Ru NCs, (d) HRTEM, and (e) HAADF-STEM image and the corresponding elemental mapping results of Ru/Nb_2O_5 after the CP test.

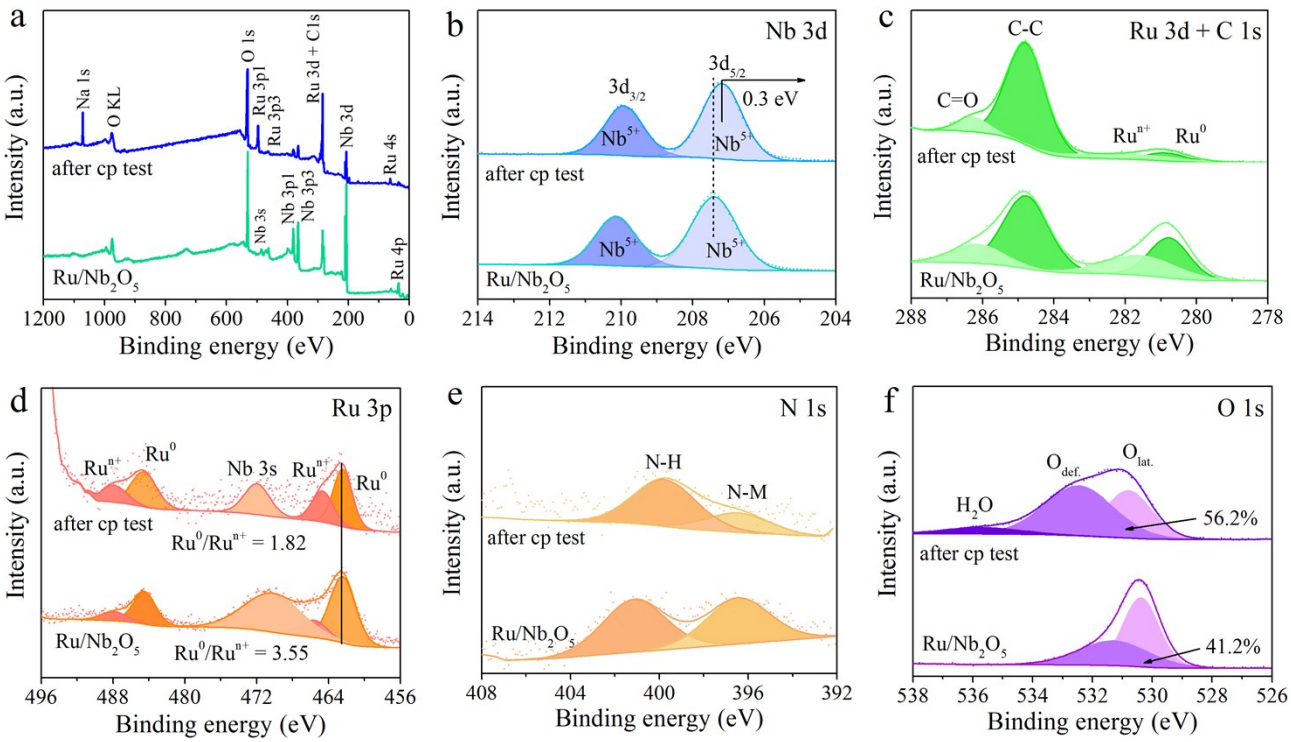

Fig. S36. (a) XPS full spectra and high resolution XPS spectra of (b) Nb 3d, (c) Ru 3d + C1s, (d) Ru 3p, (e) N 1s, and (f) O 1s for Ru/Nb_2O_5 before and after the CP test.

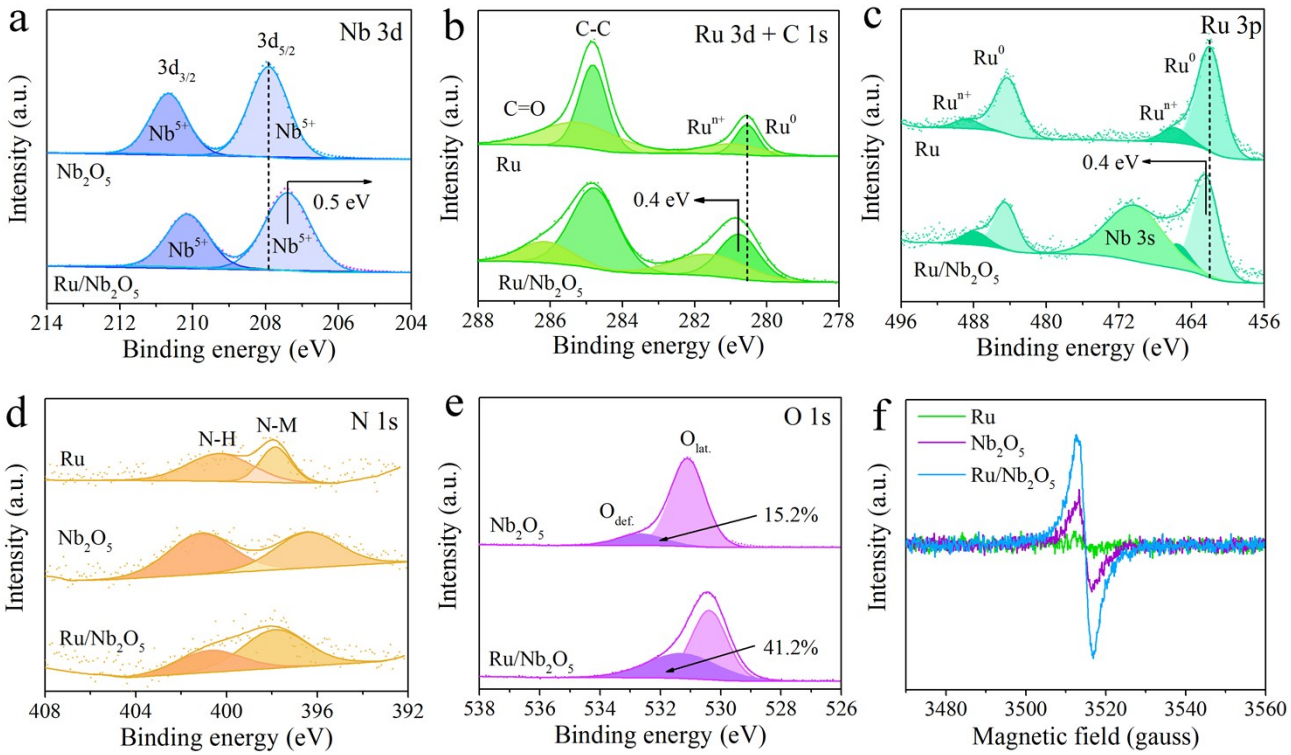

Fig. S37. High resolution XPS spectra of (a) Nb 3d, (b) Ru 3d + C 1s, (c) Ru 3p, (d) N 1s, and (e) O 1s for Ru, Nb_2O_5, and Ru/Nb_2O_5. (f) Room temperature EPR of Ru, Nb_2O_5, and Ru/Nb_2O_5.

Compared to Nb_2O_5, the binding energy of Nb $3d_{5/2}$ in Ru/Nb_2O_5 has shifted to a lower value, indicating that Nb acts as an electron acceptor (Fig. S37a). On the other hand, compared to Ru, both Ru 3d and Ru 3p in Ru/Nb_2O_5 have shifted to higher values, indicating that Ru acts as an electron donor (Fig. S37b and S37c). These results suggest that electrons are transferred from Ru to Nb_2O_5. As shown in the N 1s spectrum of the Ru/Nb_2O_5 (Fig. S37d), the peaks located at 400.7 and 397.9 eV match the N-H and N-M bonds, respectively.[24] As shown in Fig. S37e and S37f, due to the electronic interactions between Ru and Nb_2O_5, more oxygen vacancies are generated on the Ru/Nb_2O_5.

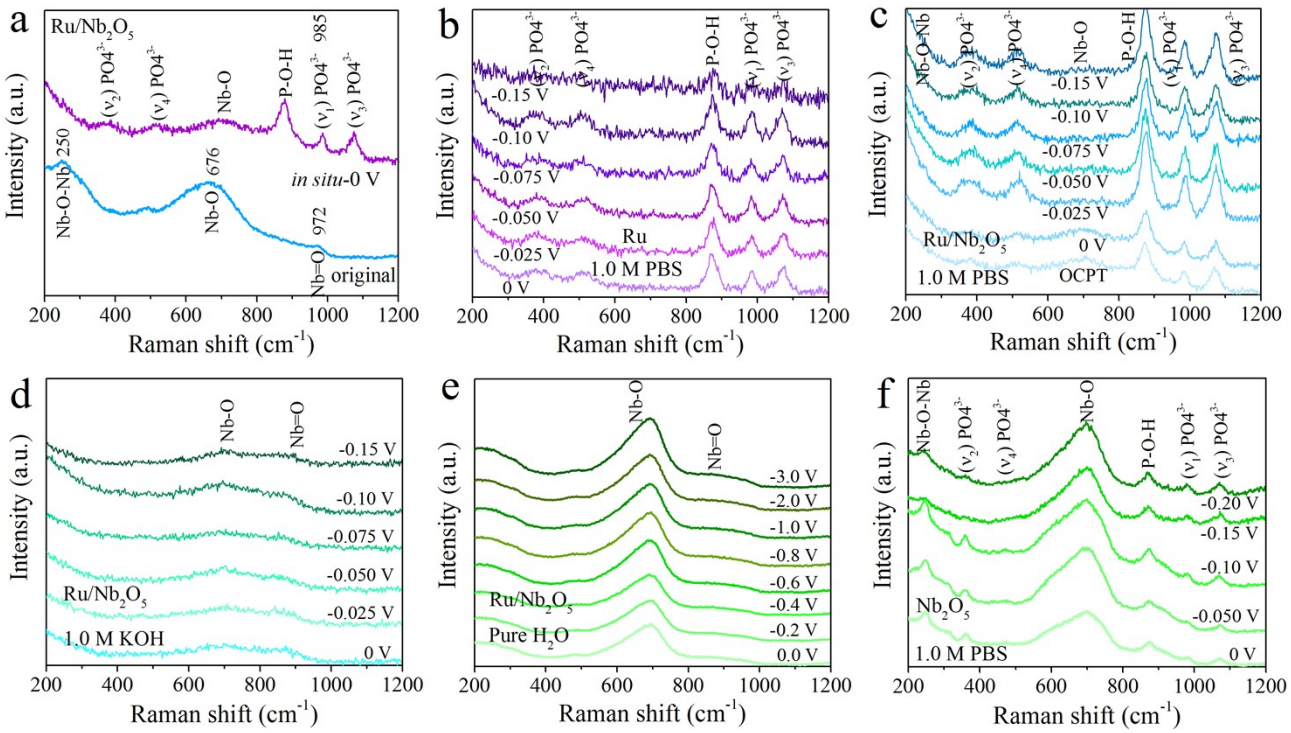

Fig. S38. (a) The *in-situ* and *ex-situ* Raman spectra of Ru/Nb_2O_5. *In situ* SERS of (b) Ru and (c) Ru/Nb_2O_5 in 1.0 M PBS. *In situ* SERS of Ru/Nb_2O_5 in (d) 1.0 M KOH and (e) pure H_2O. (f) *In situ* SERS of Nb_2O_5 in 1.0 M PBS.

In the Raman spectra of the original Ru/Nb_2O_5 sample (Fig. S38a), there are three distinct peaks located at 250, 676, and 972 cm^{-1}, which respectively correspond to Nb-O-Nb, Nb-O, and Nb=O bonds.[25, 26] In the *in-situ* spectra of Ru, only characteristic peaks belonging to phosphorus species are observed (Fig. S38b). The bands around 382, 526, 985, and 1072 cm^{-1} are associated to the symmetric (ν_2, ν_4, ν_1, and ν_3) P-O-P stretching mode of PO_4^{3-}, respectively. And the presence of bands in the region 800-900 cm^{-1} indicates the existence of P-O-H bonds forming PO_4^{3-} groups.[27, 28] During *in-situ* testing of Ru/Nb_2O_5, interference from background signals makes it difficult to detect the Nb-O-Nb bond signal, a phenomenon observed consistently in 1.0 M PBS (Fig. S38c), 1.0 M KOH (Fig. S38d), and pure H_2O (Fig. S38e). Regarding the Nb-O bond of Ru/Nb_2O_5 in 1.0 M PBS, signals can still be observed at open circuit potential (OCPT) and 0 V *vs.* RHE. However, as the

potential increases, the Nb-O bond signal gradually weakens due to interference from hydrogen gas bubbles, a phenomenon also observed in 1.0 M KOH. Due to the poor conductivity of pure water, hydrogen evolution reactions cannot occur even when the potential reaches -3.0 V *vs.* RHE. Therefore, the intensity of Nb-O and Nb=O bonds remains unaffected in pure water. However, in the *in-situ* Raman spectra of Nb_2O_5 (Fig. S38f), noticeable Nb-O-Nb and Nb-O bonds can still be observed, indicating that Ru also influences the signals to some extent. As for the Nb=O bond, interference is caused by the symmetric P-O-P stretching mode of (v_1) PO_4^{3-} at 985 cm^{-1}.

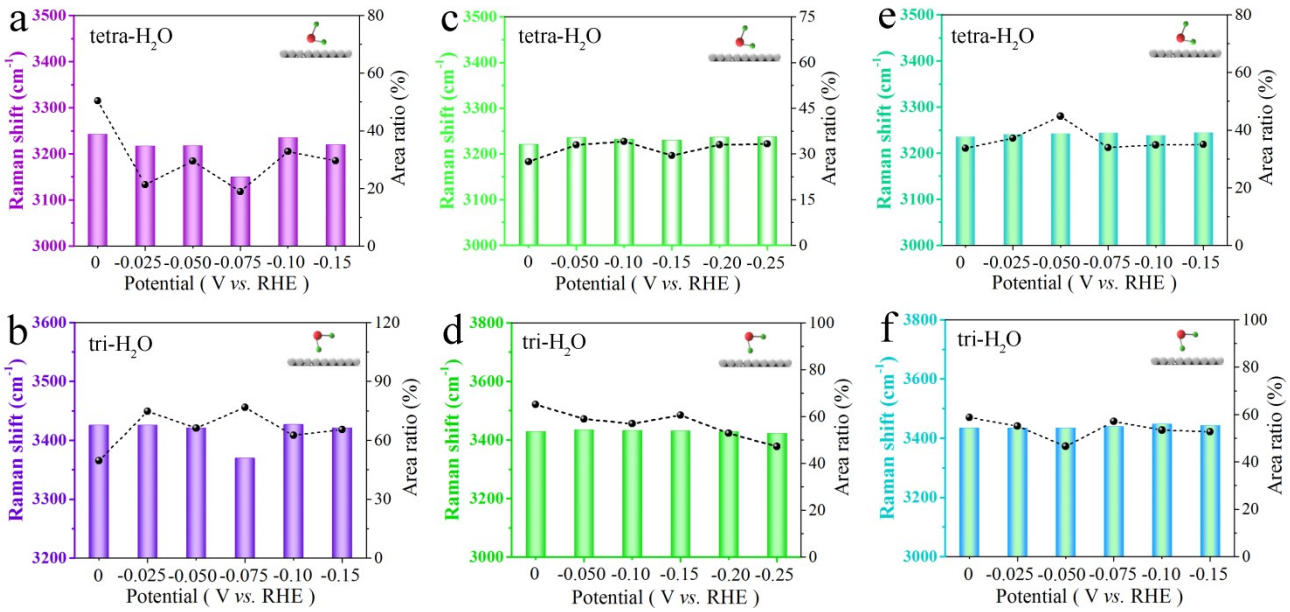

Fig. S39. Raman shifts and area ratios of the tetrahedrally coordinated and trihedrally coordinated water of the interfacial water at the (a, b) Ru, (c, d) Nb_2O_5, and (e, f) Ru/Nb_2O_5 surface.

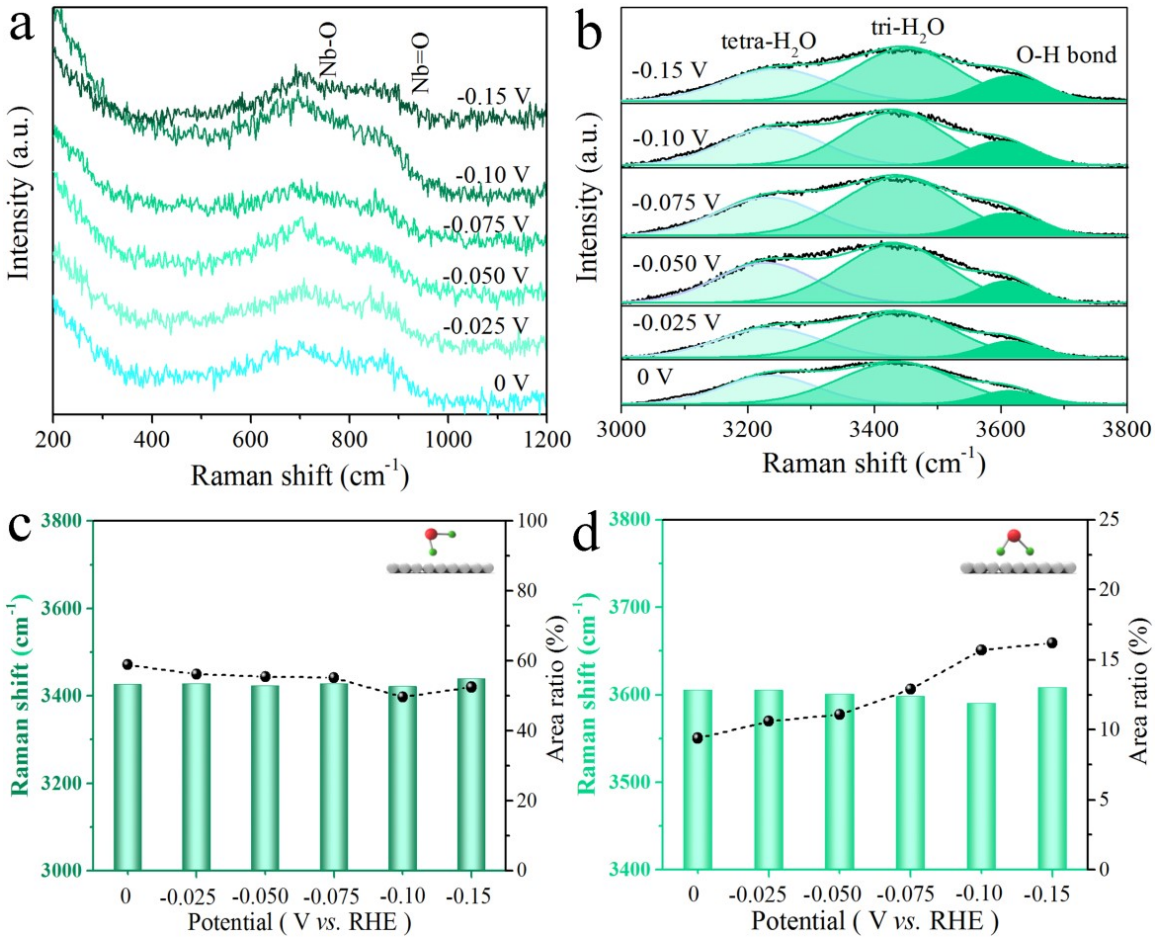

Fig. S40. *In situ* SERS of Ru/Nb_2O_5 in 1.0 M KOH in the range of (a) 200-1200 cm^{-1} and (b) 3000-3800 cm^{-1}. The corresponding Raman shifts and area ratios of the (c) trihedrally coordinated water and (d) dangling O-H bonds of the interfacial water.

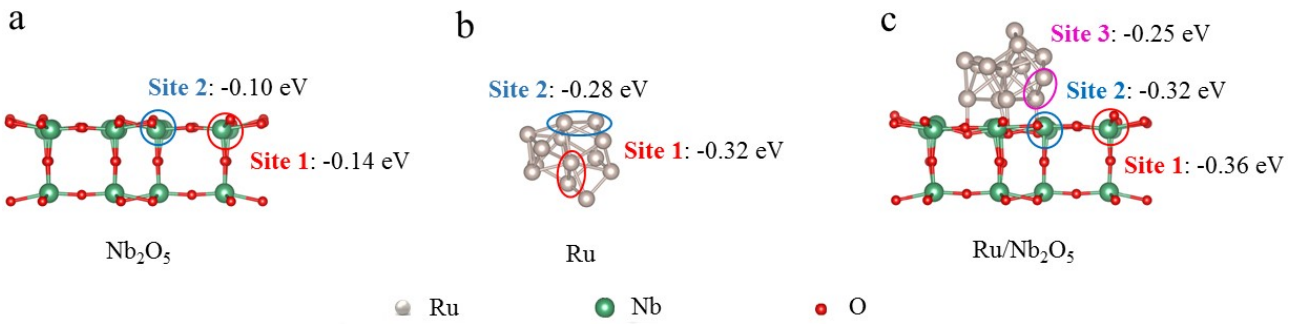

Fig. S41. Calculated ΔG_{H^*} for various sites on (a) Nb_2O_5, (b) Ru, and (c) Ru/Nb_2O_5 using the Grimme's DFT-D3 methodology to describe the dispersion interactions.

As shown in Fig. S41, we calculated the ΔG_{H^*} at different sites on Nb_2O_5, Ru, and Ru/Nb_2O_5 using the Grimme's DFT-D3 method. The adsorption strength order of H* at each site is as follows: Ru/Nb_2O_5 (Site 1 = -0.36 eV) > Ru/Nb_2O_5 (Site 2 = -0.32 eV) = Ru (Site 1 = -0.32 eV) > Ru (Site 2 = -0.28 eV) > Ru/Nb_2O_5 (Site 3 = -0.25 eV) > Nb_2O_5 (Site 1 = -0.14 eV) > Nb_2O_5 (Site 2 = -0.10 eV). Overall, Nb_2O_5 exhibits the weakest adsorption capability for H*, and on Ru/Nb_2O_5, the adsorption energy of H* at Site 3 is weaker than that on Ru. Due to the hydrogen bonding between H* and O, this binding method is not robust, and most reported studies have employed metals as active sites. Therefore, our work also chooses metals as the main active sites. Given that ideal results were not obtained at different sites, we optimized the calculation method by removing Grimme's DFT-D3 methodology.

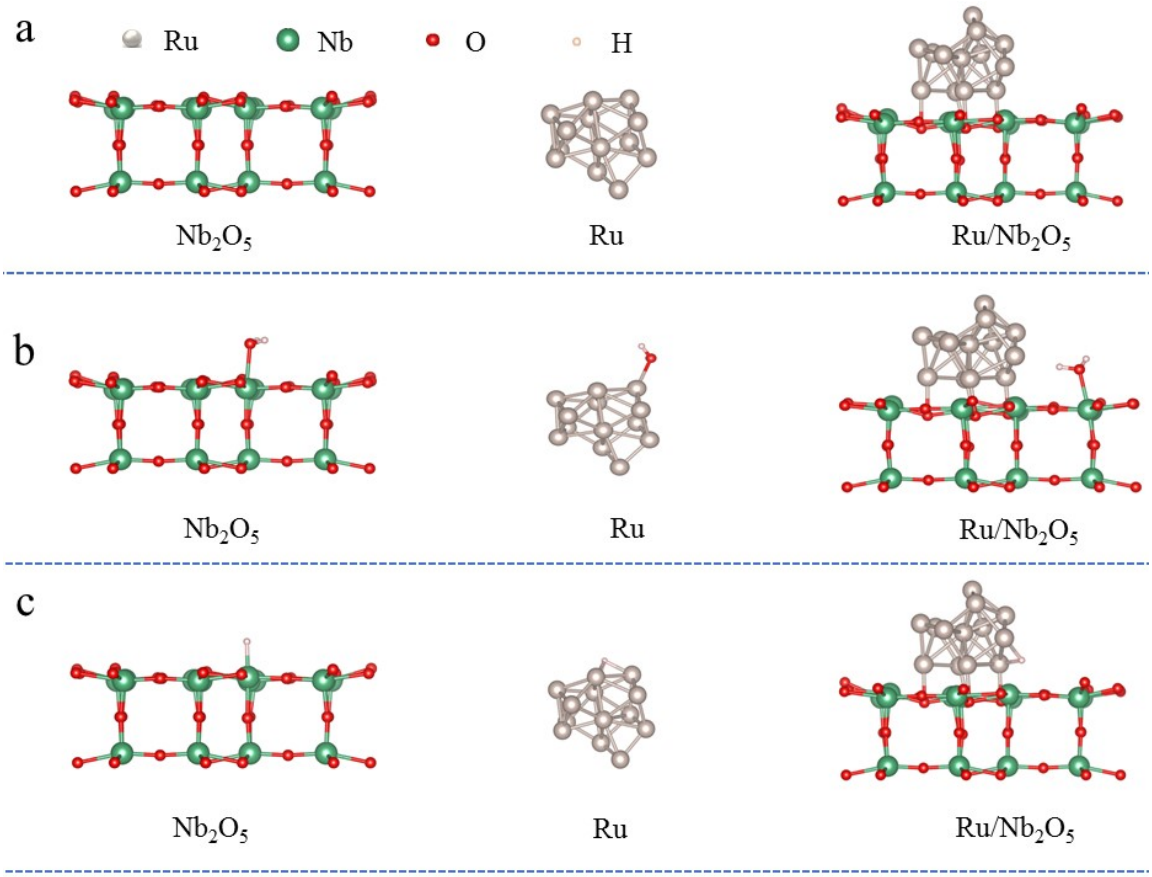

Fig. S42. (a) Structural models of the Nb_2O_5, Ru, and Ru/Nb_2O_5. Optimized structure models of (b) H_2O and (c) H* adsorbed on Nb_2O_5, Ru, and Ru/Nb_2O_5.

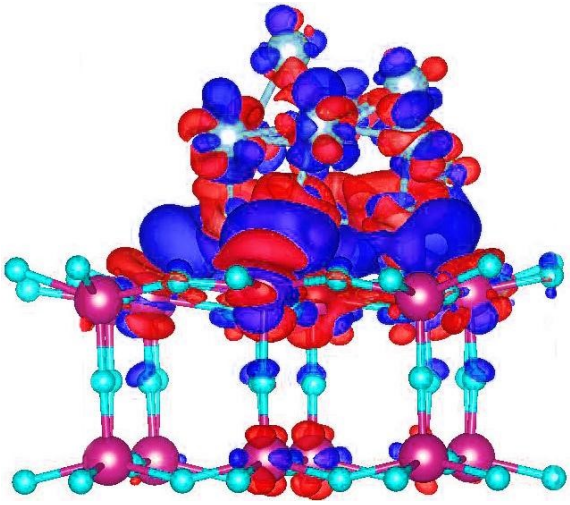

Fig. S43. The charge density difference and the average electron difference density plot of Ru/Nb_2O_5. Blue and red shadows represent electron accumulation and electron depletion regions, respectively.

Table S1. The metal content of samples Ru/Nb_2O_5 and Ru determined by ICP-MS**.**

Catalyst	Ru (wt./%)	Nb (wt./%)
Ru/Nb_2O_5	0.35	13.29
Ru	3.32 μg cm^{-2}	-

Table S2. Comparison of the catalyst mass loading and corresponding mass activity (j_m^c) of the prepared catalysts.

Catalyst	Loading amount $mg_{cat.}$ cm^{-2}	Electrolyte	j_m^c at 50 mV (mA mg^{-1})	j_m^c at 300 mV (mA mg^{-1})
Pt/C	1.60	1.0 M PBS	-12.4±1.15	-122±4.00
		1.0 M KOH	-27.6±4.26	-275±28.6
Ru/Nb_2O_5	2.08	1.0 M PBS	-9.16±1.16	-137±10.9
		1.0 M KOH	-12.9±0.887	-283±14.7
Nb_2O_5	2.00	1.0 M PBS	-0.0146±0.202	-2.76±0.213
		1.0 M KOH	-0.235±0.315	-4.11±0.398

Table S3. Comparison of the noble metal loading and corresponding mass activity (j_m) of the prepared catalysts.

Catalyst	Loading amount $\mu g_{Ru\ or\ Pt}\ cm^{-2}$	Electrolyte	j_m at 50 mV (mA μg^{-1})	j_m at 100 mV (mA μg^{-1})
Pt/C	320	1.0 M PBS	-0.0621±0.00577	-0.153±0.00853
		1.0 M KOH	-0.138±0.0213	-0.340±0.0468
Ru/Nb_2O_5	7.28	1.0 M PBS	-2.62±0.330	-8.28±0.579
		1.0 M KOH	-3.68±0.253	-14.4±1.11
Ru	3.32	1.0 M PBS	-1.40±0.181	-5.01±0.999
		1.0 M KOH	-2.32±0.702	-8.90±2.78

Table S4. C_{dl} and ECSA for CC, Nb_2O_5, Ru, Ru/Nb_2O_5, and Pt/C in 1.0 M PBS.

Catalyst	CC	Nb_2O_5	Ru	Ru/Nb_2O_5	20% Pt/C
C_{dl} (mF cm^{-2})	0.4	1.3	1.8	1.5	13.6
ECSA (cm^2)	10	32.5	45	37.5	340

Table S5. C_{dl} and ECSA for CC, Nb_2O_5, Ru, Ru/Nb_2O_5, and Pt/C in 1.0 M KOH.

Catalyst	CC	Nb_2O_5	Ru	Ru/Nb_2O_5	20% Pt/C
C_{dl} (mF cm^{-2})	0.5	1.5	2.9	1.3	16.0
ECSA (cm^2)	12.5	37.5	72.5	32.5	400

Table S6. The EIS fitting results of Ru.

Potential (V)	R_s (Ω)	R_3 (Ω)	T_3 (S•s$^{\alpha}$)	α_3
-0.025	8.053	35.70	0.0005005	0.9191
-0.050	7.975	27.95	0.0005137	0.9191
-0.075	8.076	24.86	0.0004851	0.9191
-0.100	8.005	21.80	0.0004938	0.9155
-0.125	8.076	19.18	0.0004844	0.9192
-0.150	7.907	16.64	0.0004524	0.9345
-0.175	7.950	15.17	0.0004574	0.9304

Table S7. The EIS fitting results of Ru/Nb_2O_5.

Potential (V)	R_s (Ω)	R_1 (Ω)	T_1 (S•s$^{\alpha}$)	α_1	R_3 (Ω)	T_3 (S•s$^{\alpha}$)	α_3	R_2 (Ω)	T_2 (S•s$^{\alpha}$)	α_2
-0.025	6.713	0.2247	0.001440	0.8987	1.437	0.05670	0.5941	1.646	1.052	0.9291
-0.050	6.663	0.1911	0.0004491	0.981	1.326	0.05087	0.6240	1.600	0.9279	0.7813
-0.075	6.645	0.1972	0.0007042	0.991	1.151	0.03489	0.6865	1.596	0.8530	0.6664

Table S8. The corresponding overpotentials on the CP curve and LSV curve after stability testing at different current densities (-10, -20, -50, -100, -150, and -200 mA cm^{-2}) for 12 h in 1.0 M PBS. Note: the *iR*-compensated η_{10} and η_{100} values were extracted from Fig. S32d, while the $\eta_{(Initial)}$ and $\eta_{(After\ CP\ test)}$ values without *iR*-compensation refer to Fig. 3f.

η (mV)		Initial	-10	-20	-50	-100	-150	-200
From LSV	η_{10}	31	39	59	64	66	67	54
	η_{100}	141	144	159	167	175	183	197
From CP	$\eta_{(Initial)}$	-	42	113	353	583	944	1283
	$\eta_{(After\ CP\ test)}$	-	57	137	396	644	1010	1235

Table S9. Recently reported HER catalysts used in neutral conditions.

Catalyst	Substrate	Tafel (mV dec^{-1})	η_{10} (mV)	η_{100} (mV)	j_m	Reference
$RuSe_x$-RuNC[a]	Carbon paper	53	29	-	-2.61 A mg^{-1} at 100 mV	3
Ru@NC	Glassy carbon	-	100	-	-	29
Ru_1-Ru_n/NC	Carbon paper	48	32	-	-88.9 A g^{-1} at 50 mV	30
Ru@RuO_2	Glassy carbon	50	43	~400	-77.3 mA mg^{-1} at 100 mV	20
CoRu/NC	Glassy carbon	57	30	-	-	31
Co@CNTs[b]/Ru	Glassy carbon	64	63	706	-	32
RuP_2@NPC[c]	Glassy carbon	87	57	-	-	33
Ru@Co-SAs[d]	Pt wire	82	55	-	-	34
Rh_2S_3/NC	Glassy carbon	37	46	262	-	35
PtSi	Glassy carbon	47	66	-	-	36
Pt@CoO_x	Cu foil	52	82	423	-	37
OsP_2@NPC	Glassy carbon	82	54	-	-0.43 mA μg^{-1} at 70 mV	38
OsP/PHMCSs[e]	Glassy carbon	66	56	-	-	39
NiS–Ni_2P/Ni	Nickel foam	66	115	~440	-	40
Co-NCNTs/MoS_2	Carbon cloth	96	84	~300	-	41
WS_2/Co_9S_8/Co_4S_3	Glassy carbon	126	208	-	-	42
Co_3O_4@NiCu	Nickel foam	109	73	~600	-	43
Bi–B/BiB_3O_6	Nickel foam	54	88	~450	-	44
MoO_2/MoS_2/C	Nickel foam	53	97	~300	-	45
Ni_2P/CoP	Nickel foam	73	65	~175	-	46
MoP/CNT	Carbon paper	115	102	~230	-	47

Mn-doped NiS_2	Nickel foam	65	84	~250	-71.5 A g^{-1} at 70 mV	[48]
Ru-NiFeP	Nickel foam	83	105	-	-	[49]
CoP	Carbon cloth	93	45	~300	-	[50]
Ru-MoS_2	Carbon cloth	-	114	-	-	[51]
h-$RuSe_2$	Glassy carbon	139	119	-	-	[52]
CoP@BCN[f]	Glassy carbon	59	122	-	-	[53]
CoP/NiCoP/NC	Glassy carbon	78	123	~350	-	[54]
Co-NCNT[g]	Carbon cloth	97	170	~300	-	[55]
np-CoP NWs[h]	Ti substrate	125	178	-	-	[56]
Co-Fe-P	Glassy carbon	138	138	-	-	[57]
2H-MoS_2	Carbon paper	73	142	~200	-	[58]
Ru-S-Sb	Carbon paper	118	153	-	-	[59]
Cu@WC	Cu foam	118	173	~400	-	[60]
MoS_2 NWs[i]	Carbon paper	105	188	~340	-	[61]
RuP_2@NC	Glassy carbon	116	196	-	-	[62]
Ru SAs-Ni_2P	Glassy carbon	-	260	-	-	[63]
CoNC/GD[j]	Glassy carbon	207	368	-	-	[64]
NiRu@NC	Glassy carbon	-	482	-	-	[65]
Ru/Mo_2CT_x	Glassy carbon	57	73	-	-	[21]
RuO_2-RuP_2/Ru	Glassy carbon	30	86	-	-	[66]
Ru-WO_{3-x}	Carbon paper	41	19	~90	-	[67]
$Pt_{0.47}$-Ru/Acet[k]	Nickel foam	94	8	-	-0.85 A·mg^{-1} at 100 mV	[68]
RuIr alloy	Carbon paper	19	16	150	-	[69]
V_o[l]-WO_3/Ru SAs	Carbon cloth	92	64	-	-	[70]
Co_5Ru_1	Glassy carbon	71	28	187	-	[71]
$Co_{0.87}Ru_{0.13}$/GC[m]	Carbon paper	43	39	-	2557.2 A g^{-1} at 50 mV	[72]

Ru-Co_xP	Carbon cloth	52	22	113	-	[73]
Ru/Nb_2O_5	Carbon cloth	31	33	141	8.28±0.579 mA μg^{-1} at 100 mV	This work

[a] NC: N-doped carbon; [b] CNTs: carbon nanotubes; [c] NPC: N,P dual-doped carbon; [d] SAs: single atoms; [e] PHMCSs: P-modified hollow mesoporous carbon spheres; [f] BCN: B/N co-doped graphene nanotubes; [g] NCNT: N-doped carbon nanotubes; [h] NWAs: nanowire arrays; [i] NWs: nanowires; [j] GD: graphdiyne nanosheet; [k] Acet: acetylene black; [l] V_o: oxygen vacancy; [m] GC: graphitic carbon.

Table S10. Summary of deconvoluted XPS peaks of Nb_2O_5 and Ru/Nb_2O_5 for Nb 3d.

Catalyst	$3d_{3/2}$ (eV)	$3d_{5/2}$ (eV)
Nb_2O_5	210.7	207.9
Ru/Nb_2O_5	210.1	207.4

Table S11. Summary of deconvoluted XPS peaks of Ru and Ru/Nb_2O_5 for Ru 3p.

Catalyst	$3p_{1/2}$ (eV)			$3p_{3/2}$ (eV)	
	Ru^{n+}	Ru^0	Nb 3s	Ru^{n+}	Ru^0
Ru	488.8	484.3	—	465.8	462.0
Ru/Nb_2O_5	487.9	484.5	470.2	465.6	462.4

Table S12. Summary of deconvoluted XPS peaks of Ru and Ru/Nb_2O_5 for Ru 3d and C 1s.

Catalyst	C 1s (eV)		Ru 3d (eV)	
	C=O	C−C	Ru^{n+}	Ru^0
Ru	285.2	284.8	280.9	280.6
Ru/Nb_2O_5	286.1	284.8	281.6	280.8

Table S13. Summary of deconvoluted XPS peaks of Ru, Nb_2O_5, and Ru/Nb_2O_5 for O 1s.

Catalyst	Lattice oxygen (eV)	Oxygen deficiency (eV)
Nb_2O_5	531.1	532.6
Ru/Nb_2O_5	530.4	531.3

Table S14. Summary of deconvoluted XPS peaks of Ru, Nb_2O_5, and Ru/Nb_2O_5 for N 1s.

Catalyst	N-H (eV)	N-M (eV)
Ru	400.3	397.8
Nb_2O_5	401.1	396.4
Ru/Nb_2O_5	400.7	397.9

Table S15. The surface content of each element on Ru, Nb_2O_5, and Ru/Nb_2O_5 obtained from XPS measurements.

Catalyst	Ru (at.%)	Nb (at.%)	O (at.%)	N (at.%)	C (at.%)
Ru	6.91	-	5.14	1.71	86.24
Nb_2O_5	-	17.28	48.61	7.44	26.68
Ru/Nb_2O_5	6.31	9.62	28.37	3.98	51.71

References

1. Z. Ren, Y. Han, N. Cong, L. Jin, L. Tan, H. Chen, C. Zhai, X. Zhou, H. Fang and Y. Zhu, *J. Electroanal. Chem.*, 2019, **848**, 113320.
2. L. Wu, L. Su, Q. Liang, W. Zhang, Y. Men and W. Luo, *ACS Catal.*, 2023, **13**, 4127-4133.
3. K. Sun, X. Wu, Z. Zhuang, L. Liu, J. Fang, L. Zeng, J. Ma, S. Liu, J. Li, R. Dai, X. Tan, K. Yu, D. Liu, W.-C. Cheong, A. Huang, Y. Liu, Y. Pan, H. Xiao and C. Chen, *Nat. Commun.*, 2022, **13**, 6260.
4. T. D. Kühne, M. Iannuzzi, M. Del Ben, V. V. Rybkin, P. Seewald, F. Stein, T. Laino, R. Z. Khaliullin, O. Schütt, F. Schiffmann, D. Golze, J. Wilhelm, S. Chulkov, M. H. Bani-Hashemian, V. Weber, U. Borštnik, M. Taillefumier, A. S. Jakobovits, A. Lazzaro, H. Pabst, T. Müller, R. Schade, M. Guidon, S. Andermatt, N. Holmberg, G. K. Schenter, A. Hehn, A. Bussy, F. Belleflamme, G. Tabacchi, A. Glöß, M. Lass, I. Bethune, C. J. Mundy, C. Plessl, M. Watkins, J. VandeVondele, M. Krack and J. Hutter, *J. Chem. Phys.*, 2020, **152**, 194103.
5. J. M. Ugalde, C. Sarasola and M. Aguado, *J. Phys. B: At. Mol. Opt. Phys.*, 1994, **27**, 423.
6. G. Kresse and J. Furthmüller, *Phys. Rev. B*, 1996, **54**, 11169-11186.
7. J. P. Perdew, K. Burke and M. Ernzerhof, *Phys. Rev. Lett.*, 1996, **77**, 3865-3868.
8. G. Kresse and D. Joubert, *Phys. Rev. B*, 1999, **59**, 1758-1775.
9. P. E. Blöchl, *Phys. Rev. B*, 1994, **50**, 17953-17979.
10. S. Grimme, J. Antony, S. Ehrlich and H. Krieg, *J. Chem. Phys.*, 2010, **132**, 154104.
11. H. Yang, R. Xu, Y. Gong, Y. Yao, L. Gu and Y. Yu, *Nano Energy*, 2018, **48**, 448-455.
12. F. Shen, Z. Sun, L. Zhao, Y. Xia, Y. Shao, J. Cai, S. Li, C. Lu, X. Tong, Y. Zhao, J. Sun and Y. Shao, *J. Mater. Chem. A*, 2021, **9**, 14534-14544.
13. L. Lee, B. Kang, S. Han, H.-e. Kim, M. D. Lee and J. H. Bang, *Small*, 2018, **14**, 1801124.
14. D. Liu, C. Wang, Y. Yu, B.-H. Zhao, W. Wang, Y. Du and B. Zhang, *Chem*, 2019, **5**, 376-389.
15. Z. Chen, Z. Wu, J. Xu, R. Zhao, X. Han, J. Jiang, M. Shao, B. Dong and Z. Kang, *Appl. Catal. B Environ. Energy*, 2022, **319**, 121914.
16. X. Shi, Y. Zhang, G. Xu, S. Guo, A. Pan, J. Zhou and S. Liang, *Sci. Bull.*, 2020, **65**, 2014-2021.
17. M. Yang, S. Li and J. Huang, *ACS Appl. Mater. Interfaces*, 2021, **13**, 39501-39512.
18. T. Chao, W. Xie, Y. Hu, G. Yu, T. Zhao, C. Chen, Z. Zhang, X. Hong, H. Jin, D. Wang, W.

Chen, X. Li, P. Hu and Y. Li, *Energy Environ. Sci.*, 2024, **17**, 1397-1406.

19. S. Xu, S. Feng, Y. Yu, D. Xue, M. Liu, C. Wang, K. Zhao, B. Xu and J.-N. Zhang, *Nat. Commun.*, 2024, **15**, 1720.
20. Z. Li, J. Zou, T. Liang, X. Song, Z. Li, J. Wen, M. Peng, X. Zeng, H. Huang and H. Wu, *Chem. Eng. J.*, 2023, **460**, 141672.
21. Y. Wu, L. Wang, T. Bo, Z. Chai, J. K. Gibson and W. Shi, *Adv. Funct. Mater.*, 2023, **33**, 2214375.
22. R. Šimpraga, G. Tremiliosi-Filho, S. Y. Qian and B. E. Conway, *J. Electroanal. Chem.*, 1997, **424**, 141-151.
23. D. A. Harrington and B. E. Conway, *Electrochim. Acta*, 1987, **32**, 1703-1712.
24. B. Zhang, J. Wang, J. Liu, L. Zhang, H. Wan, L. Miao and J. Jiang, *ACS Catal.*, 2019, **9**, 9332-9338.
25. Q. Deng, F. Chen, S. Liu, A. Bayaguud, Y. Feng, Z. Zhang, Y. Fu, Y. Yu and C. Zhu, *Adv. Funct. Mater.*, 2020, **30**, 1908665.
26. R. Brayner and F. Bozon-Verduraz, *Phys. Chem. Chem. Phys.*, 2003, **5**, 1457-1466.
27. G. Cheng, C. Deng, C. Wu, H. Yin, Y. Ruan, Y. Sun, Q. Xie and X. Wu, *Mater. Lett.*, 2019, **235**, 236-238.
28. P. Kolandaivel, R. Parthipan and S. Selvasekarapandian, *Cryst. Res. Technol*, 1993, **28**, 1139-1145.
29. J. Wang, Z. Wei, S. Mao, H. Li and Y. Wang, *Energy Environ. Sci.*, 2018, **11**, 800-806.
30. Y. Liu, J. Wu, Y. Zhang, X. Jin, J. Li, X. Xi, Y. Deng, S. Jiao, Z. Lei, X. Li and R. Cao, *ACS Appl. Mater. Interfaces*, 2023, **15**, 14240-14249.
31. J. Chen, J. Huang, Y. Zhao, L. Cao, K. Kajiyoshi, Y. Liu, Z. Li and Y. Feng, *Chem. Eng. J.*, 2022, **450**, 138026.
32. J. Chen, Y. Ha, R. Wang, Y. Liu, H. Xu, B. Shang, R. Wu and H. Pan, *Nano-Micro Lett.*, 2022, **14**, 186.
33. Z. Pu, I. S. Amiinu, Z. Kou, W. Li and S. Mu, *Angew. Chem. Int. Ed.*, 2017, **56**, 11559-11564.
34. S. Yuan, Z. Pu, H. Zhou, J. Yu, I. S. Amiinu, J. Zhu, Q. Liang, J. Yang, D. He, Z. Hu, G. Van Tendeloo and S. Mu, *Nano Energy*, 2019, **59**, 472-480.
35. C. Zhang, H. Liu, Y. Liu, X. Liu, Y. Mi, R. Guo, J. Sun, H. Bao, J. He, Y. Qiu, J. Ren, X.

Yang, J. Luo and G. Hu, *Small Methods*, 2020, **4**, 2000208.

36. Z. Pu, T. Liu, G. Zhang, Z. Chen, D.-S. Li, N. Chen, W. Chen, Z. Chen and S. Sun, *Adv. Energy Mater.*, 2022, **12**, 2200293.
37. L. Zhai, X. She, L. Zhuang, Y. Li, R. Ding, X. Guo, Y. Zhang, Y. Zhu, K. Xu, H. J. Fan and S. P. Lau, *Angew. Chem. Int. Ed.*, 2022, **61**, e202116057.
38. L. Fang, Y. Wang, X. Yang, H. Zhang and Y. Wang, *J. Catal.*, 2019, **370**, 404-411.
39. M. Liu, K. Shi, Z. Duan, M. Zhang, Y. Xu, Z. Wang, X. Li, L. Wang and H. Wang, *J. Mater. Chem. A*, 2022, **10**, 13042-13047.
40. M. Liu, Z. Sun, C. Zhang, S. Li, C. He, Y. Liu and Z. Zhao, *J. Mater. Chem. A*, 2022, **10**, 13410-13417.
41. J. Zhou, T. K. Leung, Z. Peng, X. Li, K. Chen, J. Yuan and M. K. H. Leung, *Small*, 2023, **19**, 2300441.
42. L. Xia, F. Wang, K. Pan, B. Zhang, W. Li, X. Ma, T. Yang, Y. Xu, Y. Ren, H. Yu and S. Wei, *ACS Appl. Mater. Interfaces*, 2023, **15**, 11765-11776.
43. S. Ma, P. Yang, J. Chen, Z. Wu, X. Li and H. Zhang, *J. Colloid Interface Sci.*, 2023, **642**, 604-611.
44. J. Fan, W. Hao, C. Fu, Z. Chen, R. Liang, C. Lian, Q. Zhang and G. Li, *J. Mater. Chem. A*, 2022, **10**, 1535-1546.
45. F. Gong, M. Liu, S. Ye, L. Gong, G. Zeng, L. Xu, X. Zhang, Y. Zhang, L. Zhou, S. Fang and J. Liu, *Adv. Funct. Mater.*, 2021, **31**, 2101715.
46. Y. Tan, J. Feng, L. Kang, L. Liu, F. Zhao, S. Zhao, D. J. L. Brett, P. R. Shearing, G. He and I. P. Parkin, *Energy Environ. Mater. 2023, **6**, e12398.*
47. X. Zhang, X. Yu, L. Zhang, F. Zhou, Y. Liang and R. Wang, *Adv. Funct. Mater.*, 2018, **28**, 1706523.
48. L. Zeng, Z. Liu, K. Sun, Y. Chen, J. Zhao, Y. Chen, Y. Pan, Y. Lu, Y. Liu and C. Liu, *J. Mater. Chem. A*, 2019, **7**, 25628-25640.
49. Y. Lin, M. Zhang, L. Zhao, L. Wang, D. Cao and Y. Gong, *Appl. Surf. Sci.*, 2021, **536**, 147952.
50. J. Tian, Q. Liu, A. M. Asiri and X. Sun, *J. Am. Chem. Soc.*, 2014, **136**, 7587-7590.
51. D. Wang, Q. Li, C. Han, Z. Xing and X. Yang, *Appl. Catal. B Environ. Energy*, 2019, **249**, 91-97.

52. Y. Zhao, H. Cong, P. Li, D. Wu, S. Chen and W. Luo, *Angew. Chem. Int. Ed.*, 2021, **60**, 7013-7017.
53. H. Tabassum, W. Guo, W. Meng, A. Mahmood, R. Zhao, Q. Wang and R. Zou, *Adv. Energy Mater.*, 2017, **7**, 1601671.
54. R. Boppella, J. Tan, W. Yang and J. Moon, *Adv. Funct. Mater.*, 2019, **29**, 1807976.
55. Z. Xing, Q. Liu, W. Xing, A. M. Asiri and X. Sun, *ChemSusChem*, 2015, **8**, 1850-1855.
56. S. Gu, H. Du, A. M. Asiri, X. Sun and C. M. Li, *Phys. Chem. Chem. Phys.*, 2014, **16**, 16909-16913.
57. J. Chen, J. Liu, J.-Q. Xie, H. Ye, X.-Z. Fu, R. Sun and C.-P. Wong, *Nano Energy*, 2019, **56**, 225-233.
58. J. Qin, C. Xi, R. Zhang, T. Liu, P. Zou, D. Wu, Q. Guo, J. Mao, H. Xin and J. Yang, *ACS Catal.*, 2021, **11**, 4486-4497.
59. Y. Li, J. Chen, J. Huang, Y. Hou, L. Lei, W. Lin, Y. Lian, X. Zhonghua, H.-H. Yang and Z. Wen, *Chem. Commun.*, 2019, **55**, 10884-10887.
60. M. Yao, B. Wang, B. Sun, L. Luo, Y. Chen, J. Wang, N. Wang, S. Komarneni, X. Niu and W. Hu, *Appl. Catal. B Environ. Energy*, 2021, **280**, 119451.
61. X. Zhang, F. Zhou, W. Pan, Y. Liang and R. Wang, *Adv. Funct. Mater.*, 2018, **28**, 1804600.
62. B.-Y. Guo, X.-Y. Zhang, J.-Y. Xie, Y.-H. Shan, R.-Y. Fan, W.-L. Yu, M.-X. Li, D.-P. Liu, Y.-M. Chai and B. Dong, *J. Hydrogen Energy*, 2021, **46**, 7964-7973.
63. K. Wu, K. Sun, S. Liu, W.-C. Cheong, Z. Chen, C. Zhang, Y. Pan, Y. Cheng, Z. Zhuang, X. Wei, Y. Wang, L. Zheng, Q. Zhang, D. Wang, Q. Peng, C. Chen and Y. Li, *Nano Energy*, 2021, **80**, 105467.
64. Y. Xue, J. Li, Z. Xue, Y. Li, H. Liu, D. Li, W. Yang and Y. Li, *ACS Appl. Mater. Interfaces*, 2016, **8**, 31083-31091.
65. Y. Xu, S. Yin, C. Li, K. Deng, H. Xue, X. Li, H. Wang and L. Wang, *J. Mater. Chem. A*, 2018, **6**, 1376-1381.
66. Y. Zhao, X. Zhang, Y. Gao, Z. Chen, Z. Li, T. Ma, Z. Wu, L. Wang and S. Feng, *Small*, 2022, **18**, 2105168.
67. J. Chen, C. Chen, M. Qin, B. Li, B. Lin, Q. Mao, H. Yang, B. Liu and Y. Wang, *Nat. Commun.*, 2022, **13**, 5382.

68. Y. Chen, J. Li, N. Wang, Y. Zhou, J. Zheng and W. Chu, *Chem. Eng. J.*, 2022, **448**, 137611.
69. Y. Jiang, Y. Mao, Y. Jiang, H. Liu, W. Shen, M. Li and R. He, *Chem. Eng. J.*, 2022, **450**, 137909.
70. J. Li, C. Zhang, C. Zhang, H. Ma, Y. Yang, Z. Guo, Y. Wang and H. Ma, *Chem. Eng. J.*, 2022, **430**, 132953.
71. J. Jiao, N.-N. Zhang, C. Zhang, N. Sun, Y. Pan, C. Chen, J. Li, M. Tan, R. Cui, Z. Shi, J. Zhang, H. Xiao and T. Lu, *Adv. Sci.*, 2022, **9**, 2200010.
72. S. Zhang, Y. Rui, X. Zhang, R. Sa, F. Zhou, R. Wang and X. Li, *Chem. Eng. J.*, 2021, **417**, 128047.
73. C. Wang and L. Qi, *ACS Mater. Lett.*, 2021, **3**, 1695-1701.